RESEARCH ARTICLE

Key Points:
- Oceanic detachment fault corrugations correspond to anastomosing fault slip planes localizing brittle deformation in shallow lithosphere
- Mass wasting is associated with detachment denudation and blankets its surface though shedding of material at termination
- Faulting, associated with magmatism and hydrothermalis, terminates detachments, and hydrothermalism linked systematically to detachments

Supporting Information:
- Supporting Information S1
- Table S1

Correspondence to:
J. Escartín,
escartin@ipgp.fr

Tectonic structure, evolution, and the nature of oceanic core complexes and their detachment fault zones (13°20′N and 13°30′N, Mid Atlantic Ridge)

J. Escartín[1], C. Mével[1] (ID), S. Petersen[2], D. Bonnemains[3] (ID), M. Cannat[1] (ID), M. Andreani[4], N. Augustin[2] (ID), A. Bezos[5], V. Chavagnac[6] (ID), Y. Choi[3], M. Godard[7], K. Haaga[8] (ID), C. Hamelin[8], B. Ildefonse[7] (ID), J. Jamieson[2,9] (ID), B. John[10] (ID), T. Leleu[6], C. J. MacLeod[11] (ID), M. Massot-Campos[12] (ID), P. Nomikou[13] (ID), J. A. Olive[14] (ID), M. Paquet[3] (ID), C. Rommevaux[1], M. Rothenbeck[2], A. Steinfuhrer[2], M. Tominaga[15] (ID), L. Triebe[2], R. Campos[16] (ID), N. Gracias[16] (ID), and R. Garcia[16]

[1]CNRS, Marine Geosciences Group, IPGP, Paris, France, [2]GEOMAR, Kiel, Germany, [3]Marine Geosciences Group, IPGP, Paris, France, [4]Laboratory of Geology, University of Lyon, Lyon, France, [5]Département des Sciences de la Terre et de l'Univers, University of Nantes, Nantes, France, [6]CNRS/GET, University of Toulouse, Toulouse, France, [7]Géosciences Montpellier, CNRS, University of Montpellier, Montpellier, France, [8]Department of Earth Science, University of Bergen, Bergen, Norway, [9]Earth Sciences Department, Now at Memorial University, Saint John's, Newfoundland and Labrador, Canada, [10]Department of Geology and Geophysics, University of Wyoming, Laramie, Wyoming, USA, [11]School of Earth and Ocean Sciences, Cardiff University, Cardiff, Wales, [12]Systems, Robotics & Vision Group, Universitat des Illes Balears, Palma de Majorca, Spain, [13]Faculty of Geology and Geo-Environment, University of Athens, Athens, Greece, [14]Lamont Doherty Earth Observatory, Columbia University, Palisades, New York, USA, [15]Department of Oceanography, Texas A&M University, College Station, Texas, USA, [16]Computer Vision and Robotics Group, Universitat de Girona, Girona, Spain

Abstract Microbathymetry data, in situ observations, and sampling along the 13°20′N and 13°20′N oceanic core complexes (OCCs) reveal mechanisms of detachment fault denudation at the seafloor, links between tectonic extension and mass wasting, and expose the nature of corrugations, ubiquitous at OCCs. In the initial stages of detachment faulting and high-angle fault, scarps show extensive mass wasting that reduces their slope. Flexural rotation further lowers scarp slope, hinders mass wasting, resulting in morphologically complex *chaotic terrain* between the breakaway and the denuded corrugated surface. Extension and drag along the fault plane uplifts a wedge of hangingwall material (*apron*). The detachment surface emerges along a continuous moat that sheds rocks and covers it with unconsolidated rubble, while local slumping emplaces rubble ridges overlying corrugations. The detachment fault zone is a set of anostomosed slip planes, elongated in the along-extension direction. Slip planes bind fault rock bodies defining the corrugations observed in microbathymetry and sonar. Fault planes with extension-parallel stria are exposed along corrugation flanks, where the rubble cover is shed. Detachment fault rocks are primarily basalt fault breccia at 13°20′N OCC, and gabbro and peridotite at 13°30′N, demonstrating that brittle strain localization in shallow lithosphere form corrugations, regardless of lithologies in the detachment zone. Finally, faulting and volcanism dismember the 13°30′N OCC, with widespread present and past hydrothermal activity (Semenov fields), while the Irinovskoe hydrothermal field at the 13°20′N core complex suggests a magmatic source within the footwall. These results confirm the ubiquitous relationship between hydrothermal activity and oceanic detachment formation and evolution.

Plain Language Summary Oceanic detachments are long-lived faults that are exposed at the seafloor, often showing prominent corrugations. Detailed mapping and inset observations and sampling, using remotely operated and autonomous robots, demonstrate as these fault surfaces are exposed at the seafloor, erosion and deposition of debris cover these faults systematically with a thin layer of rubble, demonstrating that their evolutions intimately linked to surface processes. Locally, the fault itself is exposed, displaying striated fault planes on the flanks of corrugations. A complex, three-dimensional network of fault planes within the detachment zone defines elongated bodies of rock (corrugations).These detachments also confirm that there is a direct link between detachment formation and hydrothermal activity, as they host both active and inactive hydrothermal fields.

1. Introduction

Seafloor spreading involving oceanic detachment faults, recognized as a distinct mode of oceanic accretion [*Escartín and Canales*, 2010], is inherently asymmetric and widespread both at slow and ultraslow spreading

ridges [e.g., *Cannat et al.*, 2006; *John and Cheadle*, 2010; *Smith et al.*, 2006]. It also results in an oceanic lithosphere that is compositionally and tectonically complex. One of the most striking features of this mode of accretion is the long-term (up to >1 Myr) localization of strain along fault planes exposed at the seafloor as undulating, corrugated surfaces, often associated with elevated massifs [*Cann et al.*, 1997; *Tucholke et al.*, 1998] and referred to as oceanic core complexes (OCCs). These OCCs typically expose all types of eruptive and both plutonic and mantle-derived (ultramafic) rocks that are variably altered and deformed [*Dick et al.*, 2008; *Escartín et al.*, 2003a; *MacLeod et al.*, 2002], suggesting a complex history of deformation and associated fluid circulation along the fault zone. The link between deformation and hydrothermal activity is further confirmed by a robust association along the Mid-Atlantic Ridge (MAR) of oceanic detachment faults with both seismicity and hydrothermal activity [*Escartín et al.*, 2008]. To date, all the OCCs that have been explored along the Mid-Atlantic Ridge (MAR) are known to host active hydrothermal vents, show extinct hydrothermal deposits, or both (e.g., Logatchev, TAG, Semenov, Lost City, Rainbow, Ashadze, and Von Damm) [*Andreani et al.*, 2014; *Connelly et al.*, 2012; *Früh-Green et al.*, 2003; *German et al.*, 2010; *Ondréas et al.*, 2012; *Pertsev et al.*, 2012; *Petersen et al.*, 2009; *Tivey et al.*, 2003].

To understand the development of oceanic detachment faults and OCCs, and to ultimately constrain the interactions between crustal accretion and large-slip, long-term detachment faulting, in situ observations of these structures are critical. The detachment systems at Atlantis Massif and south of the Kane transform along the MAR are among the best studied of such structures, as both have been extensively explored and sampled using deep-sea vehicles [*Blackman et al.*, 2001; *Dick et al.*, 2008; *Karson et al.*, 2006; *Tucholke et al.*, 2013] and by drilling in the case of Atlantis Massif [*Blackman and Collins*, 2010; *Früh-Green et al.*, 2016; *Ildefonse et al.*, 2007]. In situ observations and samples have also been acquired at other detachments elsewhere along the MAR (e.g., TAG, Logatchev, 15°45′N at MAR), as well as along other mid-ocean ridges (e.g., Mt Dent on the mid-Cayman Rise, Fuji Dome, and Atlantis Bank along the southwest Indian Ridge, and Godzilla along a back-arc ridge), but they are less well studied. However, the Kane area hosts several fossil detachment systems, and Atlantis Massif is likely inactive, with a major rift valley bounding fault dissecting its corrugated surface, as suggested also by microseismicity in the area [*Collins et al.*, 2012].

In this paper, we present results from a recent cruise to the 13°20′N and 13°30′N OCCs on the MAR (Figure 1). Previous studies of this area have provided data on the morphology and seafloor characteristics [*MacLeod et al.*, 2009; *Smith et al.*, 2008, 2006], as well as the patterns of seismicity [*Escartín et al.*, 2003b; *Olive and Escartín*, 2016; *Smith et al.*, 2003], suggesting that both detachments are likely active at the present time or have been until very recently. Here we present detailed microbathymetric data acquired by an autonomous underwater vehicle (AUV), as well as detailed geologic observations and sampling conducted during remotely operated vehicle (ROV) dives. These novel observations enable direct comparisons between two adjacent OCCs, and shed new light on (a) processes operating at oceanic detachments (e.g., deformation, exhumation, fluid flow, relationship to magmatism, and hydrothermal activity), (b) structure and composition of the underlying lithosphere throughout the area, and (c) the internal structure, composition, and origin of the corrugated slip surface commonly observed on detachment footwalls. In situ sampling also enables comparisons with prior results of dredging campaigns, and to reevaluate aspects of previous geological interpretations of these tectonically and lithologically complex areas that characterize slow and ultraslow spreading segments.

2. Geological Setting and Prior Work

The 13°20′N and 13°30′N OCCs have developed on the western flank of the MAR axial rift valley, where they root. These detachments, first identified during shipboard geophysical surveys [*Smith et al.*, 2006], formed along a ridge section (between ∼12°55′N and 13°45′N) that is characterized by reduced melt supply to the ridge axis, as suggested by gravity data. This ridge section has produced over the past ∼10 Myr a corridor of oceanic crust punctuated by numerous oceanic detachment faults and associated OCCs [*Smith et al.*, 2008, 2006]. The corrugated 13°20′N and 13°30′N OCCs, which extend ∼7 and ∼12 km along axis, respectively, span ∼5.5 and ∼8 km in the spreading direction, and may record extension localized along the fault for ∼0.5 and 0.7 Myr, assuming symmetric spreading at a half-rate of 12 km/Myr. Near-bottom sonar imagery and its tectonic interpretation [*MacLeod et al.*, 2009; *Mallows and Searle*, 2012] suggested that the
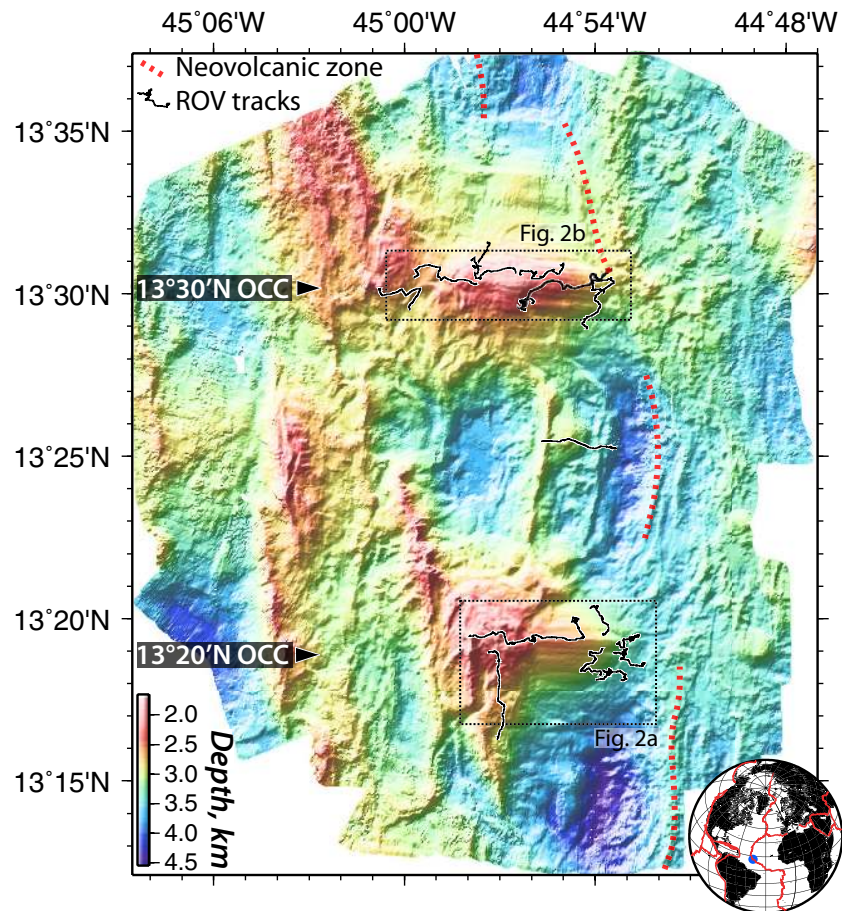
Figure 1. Shipboard bathymetry (gridded at 40 m) showing the 13°20′N and 13°30′N oceanic core complexes (OCCs), and the ROV VIC-TOR6000 tracks conducted during the ODEMAR cruise. Segments of the neovolcanic zone (red dashed lines) are located along the center of acoustically reflective volcanic seafloor at the rift valley floor [*MacLeod et al.*, 2009], and confirmed by the magnetic data [*Mallows and Searle*, 2012]. Boxes correspond to AUV microbathymetry maps and sampling shown in Figure 2.

13°20′N detachment, displaying a pristine morphology, may still be active, whereas the 13°30′N detachment may be inactive owing to the recent propagation of adjacent volcanic ridges to the north, and consequent termination of the detachment fault.

Dredge, TV-grab sampling, and seafloor rock drilling at these detachments faults yielded a wide range in rock types, consistent with the exposure of deep-seated rocks (gabbro and peridotite), in addition to basalt/diabase, and including fault rocks [*MacLeod et al.*, 2009; *Pertsev et al.*, 2009]. The geochemistry of basalts recovered has been also interpreted as an indicator of a change in magmatic activity from a period of low supply of magma to the ridge axis at the initiation of detachment faulting, to more robust axial melt supply at the present time [*Wilson et al.*, 2013].

Early surveys carried out during Russian cruises located and defined several extinct hydrothermal fields throughout the 13°30′N detachment using a deep-towed self-potential system, in addition to TV-camera surveys and sampling [*Bortnikov et al.*, 2015; *Cherkashev et al.*, 2013; *Cherkashov et al.*, 2016, 2010b; *Pertsev et al.*, 2012]. These data and results clearly demonstrate that hydrothermal activity has been present in space and time throughout the exposed fault surface, from its termination near the ridge axis to the limit of the corrugated surface to the west. In addition to inactive hydrothermal fields, an active hydrothermal field (Semenov-2) was observed [*Beltenev et al.*, 2007; *Cherkashov et al.*, 2010b; *Pertsev et al.*, 2012]. Hydrothermal deposits, which yield ages of up ∼100 kyr, show no apparent progression with age (e.g., in the

direction of spreading), as older deposits are found near the axis, while the active site is >5 km off axis [*Cherkashov et al.*, 2010a].

3. Data and Methods

The ODEMAR cruise, which took place in November to December 2013 onboard N/O Pourquoi Pas? (IFREMER, France), studied the 13°20′N and 13°30′N oceanic detachment faults along the MAR (Figure 1). During the cruise, we deployed the autonomous underwater vehicle AUV Abyss (GEOMAR, Germany) to obtain microbathymetry over both detachment systems (Figure 2), in addition to water column data (nephelometry and Eh). AUV microbathymetry data were processed onboard and the resulting microbathymetric grids used to plan dives with the ROV Victor6000 (IFREMER, France), for geologic observations and sampling (Figures 1 and 2). A full cruise report is available online (www.sismer.fr).

3.1. Shipboard and AUV Multibeam Bathymetry

Multibeam bathymetry data were acquired using a 12 kHz SeaBat 7150 system onboard N/O Pourquoi Pas?, and processed at a resolution of 40 m/pixel (Figure 1), improved on the existing ∼80–100 m/pixel resolution available from prior cruises [*MacLeod et al.*, 2009; *Mallows and Searle*, 2012; *Smith et al.*, 2006].

Near-bottom bathymetry data were acquired with a 200 kHz RESON 7125 multibeam during 8 AUV Abyss dives at an average altitude of ∼70 m above seafloor. The combined AUV surveys cover ∼76 km^2 of seafloor. The AUV multibeam bathymetry data were first renavigated using the MBNAVADJUST routine (MB-System), and the data edited in QPS QINSY® to obtain an initial grid for each AUV dive. The processed data were then used to generate a single combined grid for each OCC, at a resolution of ∼2 m per pixel (Figure 2). Shipboard bathymetry data is publicly available through the Sea Scientific Open Data site (SEANOE, www.seanoe.org), and AUV microbathymetry is available upon request, and will be made publicly available in late 2017 through this same website.

3.2. ROV Sampling, Observations, and Image Surveys

We conducted 21 ROV dives (Figure 1) mostly based on targets identified in the AUV microbathymetry, which provided >210 h of video imagery along a total of ∼100 km of dive tracks. From these dives, we recovered 422 samples, of which 172 were unequivocally in situ, based on onboard dive descriptions and observations, and a postcruise review of video imagery. Of these in situ samples, 52 were reoriented onboard correlating the ROVs' video imagery of sampling sites with the samples themselves, in addition to the ROV navigation and orientation information (position, heading, pan and tilt of the camera). We estimate an orientation error of less than ∼20°.

All samples were cut and curated onboard, taking into account their orientation when available. Onboard sample descriptions were reviewed postcruise based on thin section observations, to report composition, alteration, deformation, texture, etc. Sample locations together with a lithologic summary (see below) are reported in supporting information Table S1.

We conducted systematic video surveys of selected outcrops of geological interest encountered during our VICTOR6000 dives. Video surveys fully imaged areas of interest (e.g., fault outcrops, see below) with crosscutting horizontal and vertical tracks. Video imagery was processed to generate both videomosaics and three-dimensional terrain models with a resolution of <20 cm, better than that from acoustic mapping systems. Techniques of image processing, mosaicing, and video-based terrain modeling are described elsewhere [*Nicosevici and Garcia*, 2013]. All ROV video imagery is available online (video.ifremer.fr).

3.3. Dredging

We conducted a total of 14 dredges, which yielded more than 2.5 Tn rocks. Dredge samples were initially examined on board, and classified based on rock type, structure, and alteration history. A representative set of samples of each rock type and from each dredge was cut and described in detail onboard. Descriptions and rock types were subsequently refined postcruise. A summary of rock types (see below), in addition to relevant dredge information, is given in supporting information Table S2. Both ROV and rock samples are archived and stored at IPGP, and available upon request.
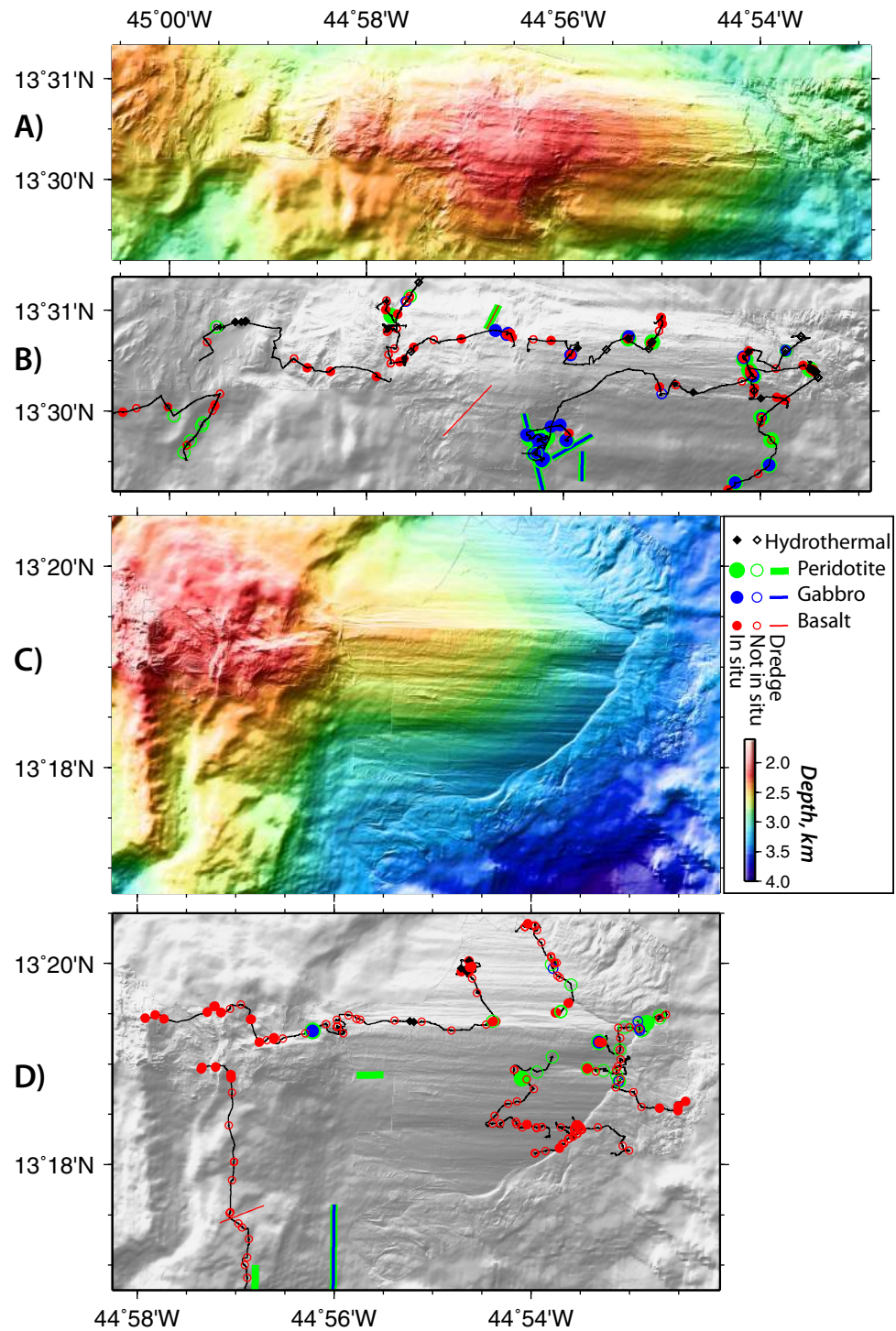
Figure 2. AUV microbathymetry (merged with shipboard bathymetry) and primary rock types of samples recovered during ODEMAR ROV dives (black thin lines) and dredges (colored lines of different thickness). (A) Microbathymetry of the 13°30′N OCC. (B) Shaded relief of the 13°30′N OCC and primary lithologies sampled. (C) Microbathymetry of the 13°20′N OCC. (D) Shaded relief of the 13°20′N OCC and primary rock types sampled. Locations of the two microbathymetric maps are shown in Figure 1. The limit of the AUV surveys is visible at the transition from the smooth shipboard bathymetry (40 × 40 m pixels) and the AUV bathymetry (2 × 2 m pixels).

3.4. Lithological Description

Rock types from both ROV sampling and dredging (reported in supporting information Tables S1 and S2, respectively) are plotted in the maps (Figure 2), and correspond to simplified sample descriptions. In this paper,

we focus on the primary lithology, as well as on the most important alteration and deformation characteristics, to understand the composition and architecture of the oceanic lithosphere. The distribution of rock types at each OCC and for each terrain described in section 4 below is also shown in supporting information Figure S2.

We have classified the samples into four primary rock types, which are briefly described below: *basalt*, *gabbro*, *peridotite*, and *hydrothermal* deposits. Some of these rocks are variably deformed and altered (including fault breccias, ultramafic-derived schists, etc.). A detailed study of deformation processes, conditions, and fluid-rock interactions within the detachment fault zone are beyond the scope of this paper and will be presented in a follow-up study (Bonnemains, et al., Pervasive silicification and hangingwall overplating along the 13°20′N oceanic detachment fault (Mid-Atlantic Ridge), submitted to *G-cubed*, 2017). Finally, the tables also report samples of unknown primary lithology (e.g., unconsolidated clay fault gouges), in addition to specific comments and observations regarding the nature of deformation and deformation conditions, alteration, volcanic features, among others.

Basalt. This rock type encompasses all extrusive and dike rocks as deciphering them is often not possible. The Comments column in supporting information Table S1 reports obvious pillow, sheet flow, and dike structures, either from the sample itself, or from outcrop observations at the sampling site. Basalts may have been brecciated or/and recrystallized; some of these breccias are of tectonic origin and associated with the detachment fault, whereas others have a sedimentary or volcanoclastic origin.

Many samples from the 13°20′N OCC have undergone greenschist facies alteration (chlorite, actinolite, albite, titanite, quartz). In some cases, pillow textures (variolitic rims) are still obvious. Brecciation is generally inferred to result from brittle deformation, although some fine-grained breccias involving pillow fragments and glassy shards can be interpreted as hyaloclastites. The greenschist facies alteration is indicated in the comments within supporting information Table S1.

Gabbro. This category covers all the plutonic rocks, from gabbro in a strict sense to felsic differentiates. Static hydrothermal recrystallization is ubiquitous, but with variable intensity (e.g., amphibole after pyroxenes and secondary plagioclase). In a few cases, felsic differentiates infiltrate mafic rocks. Some samples have undergone cataclastic deformation resulting in the transition from highly fractured gabbros with little displacement to cataclastic breccias. Ductile deformation may result in schistose rocks, namely amphibolite or chlorite schists. Given the context in which they occur, and in particular the field association with mafic and ultramafic rocks, we infer that most schists derive from gabbroic rocks, although some may derive from a basaltic protolith. In some cases, brecciated textures can still be identified. There is limited evidence for high-temperature crystal-plastic ductile deformation of the primary igneous assemblage of the gabbros, a deformation that is commonly observed at other oceanic core complexes such as Atlantis Bank or Kane [*Cannat et al.*, 1991; *Dick et al.*, 2010; *Hansen et al.*, 2013; *Miranda and John*, 2010; *Schroeder et al.*, 2007].

Peridotite. All peridotites are largely or totally serpentinized. Most rocks show serpentinization textures that indicate static conditions of hydration (e.g., mesh textures). Interaction between peridotite and magma is also recorded in samples infiltrated by gabbroic melts or crosscut by basaltic dikes. Some samples showing ductile deformation of secondary phases result in both talc and serpentinite schists. Samples diplaying alternating bands of both amphibolite/chlorite schists and serpentine/talc schists are interpreted as sheared gabbro/peridotite contacts.

Hydrothermal. This category covers all deposits related to both active and inactive hydrothermal discharge at the seafloor. Hydrothermal samples correspond primarily to massive sulfides from hydrothermal chimneys and mounds, and to iron hydroxides.

Other. Other rock types, such as manganese crusts and calcareous sediments that are variably lithified, are reported under a broad category named "Other" in the supporting information Table S1.

4. Tectonic Structure, Geological Observations, and Rock Types

We differentiate three distinct structural domains at both the 13°20′N and 13°30′N detachments (Figure 3), based upon microbathymetry and seafloor observations conducted during the ODEMAR cruise (Figure 1), combined with previous data collected in this area and elsewhere. Below we describe these structural domains from off axis (west) toward the ridge axis (east), with the naming used hereon in italics:

1. The *chaotic terrain*, i.e., the area between the *footwall cutoff* of the fault, often referred to as breakaway, and the limit of the *corrugated surface* away from the axis (Figures 3–5);
2. The *corrugated surface*, i.e., the surface showing microbathymetric corrugations that are parallel to spreading (Figures 3 and 6−9);
3. The *hangingwall cutoff*, where the *corrugated surface* emerges from the rift valley floor, and including the adjacent seafloor that lies between the hangingwall cutoff and the volcanic rift valley floor, referred to as *apron* from here on (Figures 3, 10 and 11).

As the 13°20′N OCC is structurally intact, we describe it in detail and then compare it with 13°30′N OCC, which is being dismembered and appears to be in the process of being terminated (Figures 3B and 3D), if not already inactive [*MacLeod et al.*, 2009]. Beyond the domal OCCs themselves, we describe two additional areas, i.e., the *axial valley floor* with recent volcanic deposits, and the e) *inter-OCC seafloor*, which corresponds to the faulted off-axis crust between the two OCCs (Figure 12). Figure 3 shows three-dimensional
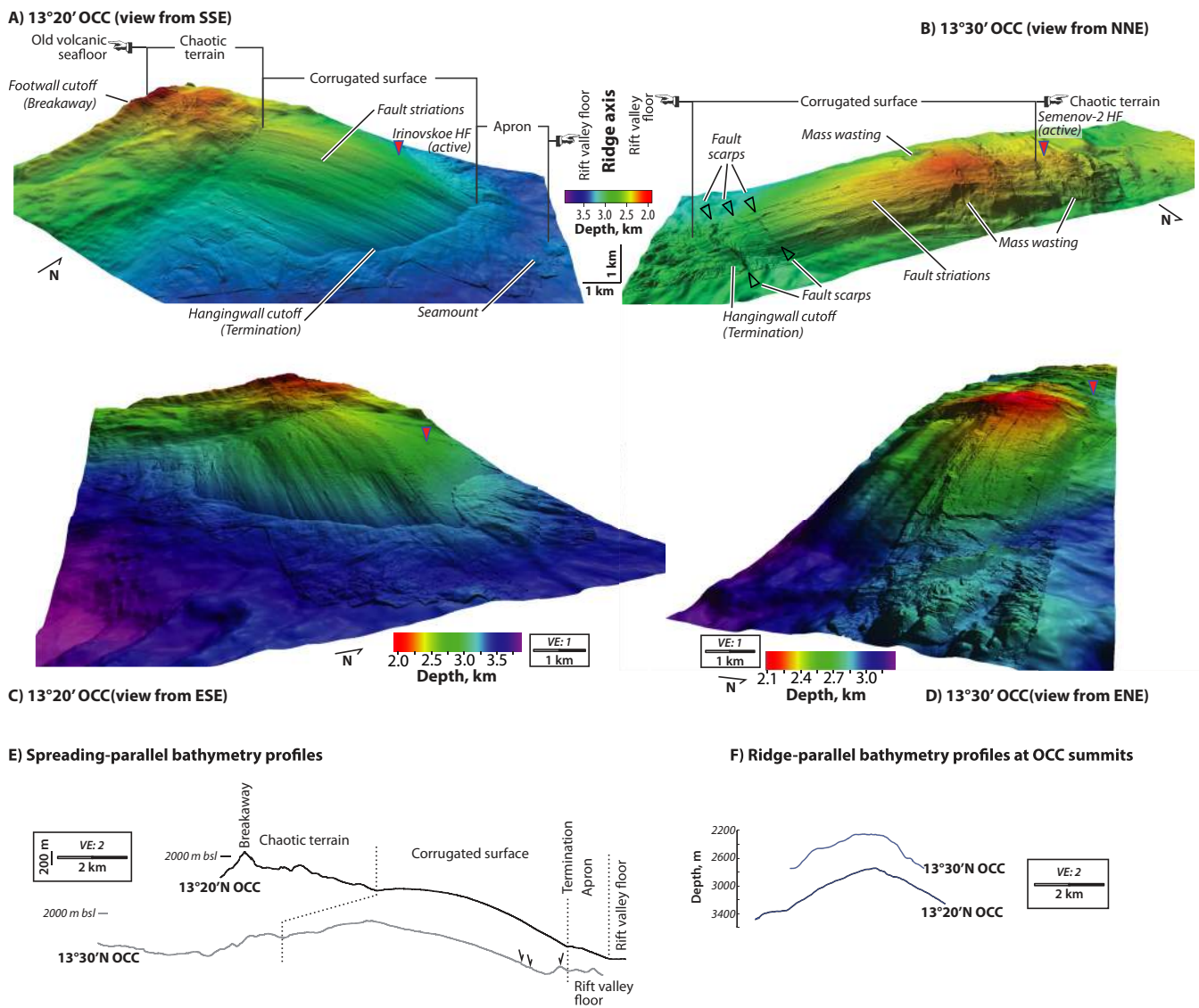

Figure 3. Three-dimensional views of (A) the 13°20′N OCC microbathymetry (Figures 2C and 2D), viewed from the SSE, and (B) the 13°30′N OCC (Figures 2A and 2B) viewed from the NNE, showing the different structural domains together with other morphologic features (all discussed in the text). Additional views from the ridge axis of both the (C) 13°20′N OCC and the (D) 13°30′N OCC are also shown. Active hydrothermal fields (HF) are indicated in the four panels (upside-down triangles, filled red). (E) Bathymetric profiles parallel to the spreading direction along the center of both detachments. Location and limits of the different terrains identified are shown. The profiles have been aligned at their terminations, and vertically offset for clarity. The 2000 m depth is indicated as a horizontal bar for each profile. (F) Bathymetric profiles parallel to the ridge axis and across the summit of both OCCs' *corrugated surface*. The along-axis profiles are shown with no offset in depth. Profiles in both Figures 3E and 3F are shown with a vertical exaggeration (VE) of 2.
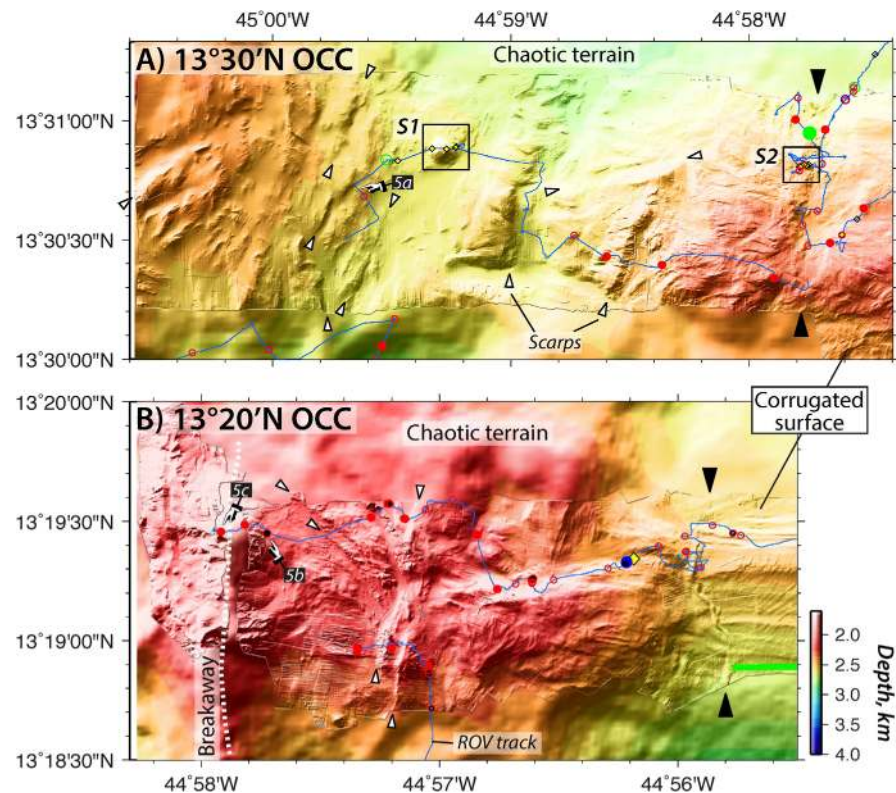
Figure 4. Detailed microbathymetry over *chaotic terrain* at the (A) 13°30′N OCC and (B) 13°20′N OCC. Rock types correspond to the legend in Figure 2. Maps show ROV tracks (blue lines), the limit between the chaotic terrain and the *corrugated surface* (large black triangles), scarps within the *chaotic terrain* (small white triangles), the position of the breakaway (dashed white line) at the 13°20′N OCC in Figure 4B. Squares labeled S1 and S2 in Figure 4A indicate the locations of the inactive Semenov-1 and the active Semenov-2 hydrothermal fields. Labels in a black box (5a–5c) refer to the location of seafloor images in Figure 5.

views of both detachments with the different structural domains and other morphological features indicated (faults, mass wasting structures, hydrothermal fields, etc.).

The *chaotic terrain*, the *corrugated surface*, and the *axial valley floor* are present both at 13°20′N and 13°30′N, while the *apron* is only observed at the active, well-preserved 13°20′N OCC. This terrain is likely masked by late faulting and mass wasting at the 13°30′N OCC (see section 6 and Figure 3). The description of the *inter-OCC seafloor* below is based on the shipboard bathymetry (Figure 1) and ROV observations and sampling solely, as we did not conduct a microbathymetric AUV survey here.

4.1. Footwall Cutoff and Chaotic Terrain

Oceanic detachment faults in the 13°N area (Figure 1) develop ridgeward from prominent linear ridges that extend ~15–20 km along axis, slightly oblique to the ridge trend [*Mallows and Searle*, 2012; *Smith et al.*, 2006]. Their outer boundaries, which structurally limit the oceanic detachments away from the ridge axis, are commonly referred to as the breakaway [*MacLeod et al.*, 2009; *Tucholke et al.*, 1998] and correspond directly to the *footwall cutoff*.

The *chaotic terrain* extends between the ridgeward edge of the linear ridge and the initiation of the *corrugated surface* (Figure 4). The *chaotic terrain* at the 13°20′N OCC has a width of ~3.5 km at the center of the OCC (Figure 4B), with the microbathymetric data indicating an overall ridgeward slope of ~8°; at the breakaway itself the slopes are of ~30°–35° toward the ridge axis and ~15°–20° away from it (Figure 3E). These slope angles are consistent with those reported earlier from profiler data acquired during sonar surveys to estimate the fault angle prior to rotation [*MacLeod et al.*, 2009]. In contrast, at the 13°30′N OCC the breakaway is not fully imaged by the microbathymetry data, but it extends over a longer distance along spreading (>5.2 km, Figures 1−3 and 4A). There the *chaotic terrain* does not show a progressive slope from the breakaway toward the ridge, and displays instead a relative low at its center.
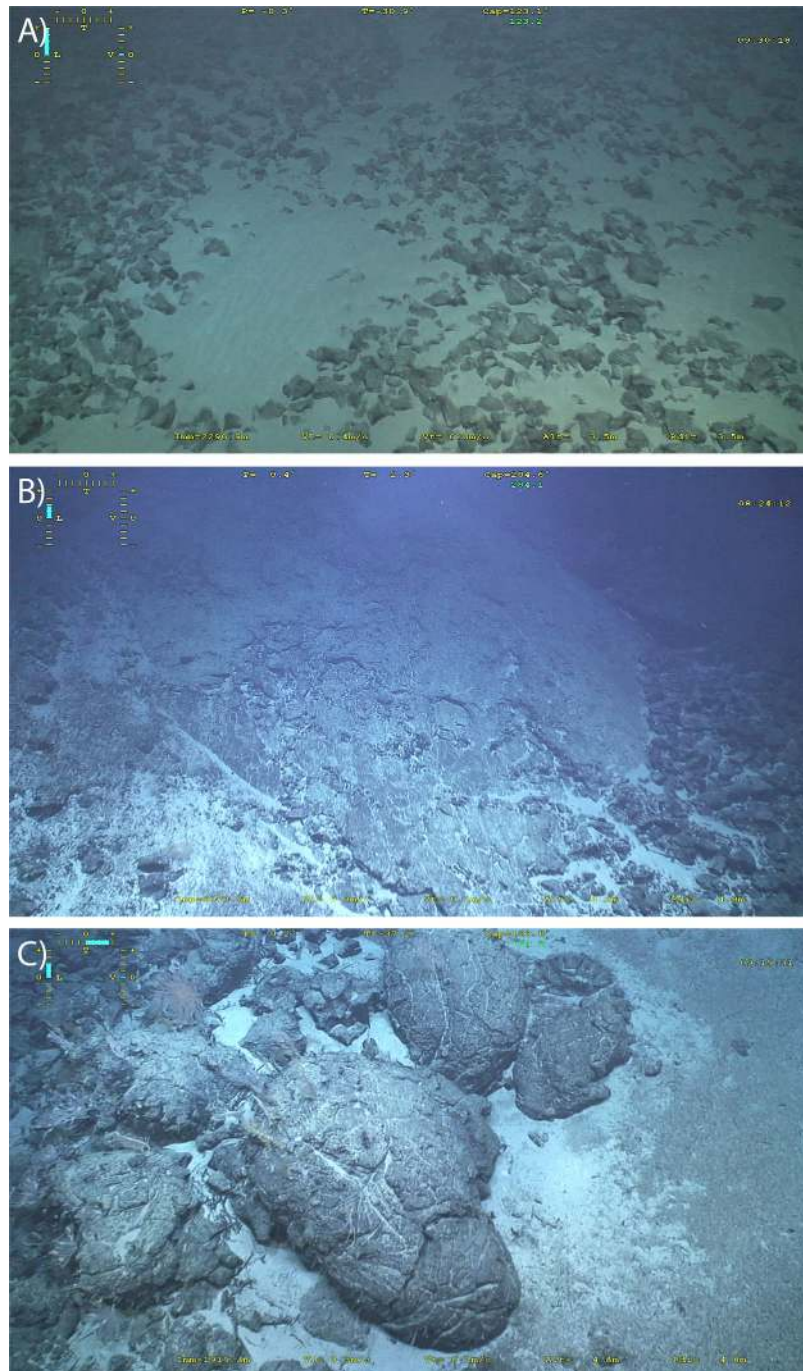
Figure 5. ROV video captures from chaotic terrain seafloor. (A) Rubble and sediment along slope facing away from the ridge axis (field of view ~15 m across, dive 446, 13°30'N OCC). (B) View of the ridgeward scarp of the breakaway, showing rubble surrounding a fault surface that dips toward the axis (field of view ~15 m, dive 555, 13°20'N OCC). (C) In situ pillow lavas on sedimented seafloor at the summit of the breakaway and that slopes westward and away from the ridge axis (field of view ~10 m, dive 555, 13°20'N OCC). The location of images along corresponding ROV tracks is shown in Figure 4.

The *chaotic terrain* associated with both OCCs are morphologically complex. Most of the topographic slopes are gentle (<20°) and define short scarps, extending laterally from a few hundreds of m to a maximum of a few km, with no clear regional pattern. At 13°20'N, we observe greater scarp heights that face away from the ridge axis, often curved in plan view (Figure 4B). Geological observations during ROV dives confirms the complex nature of these domains, showing banks of talus with angular basaltic blocks, heavily sedimented areas with floating blocks, trails of angular blocks, and rubble-covered slopes (Figure 5A). While sonar data showed
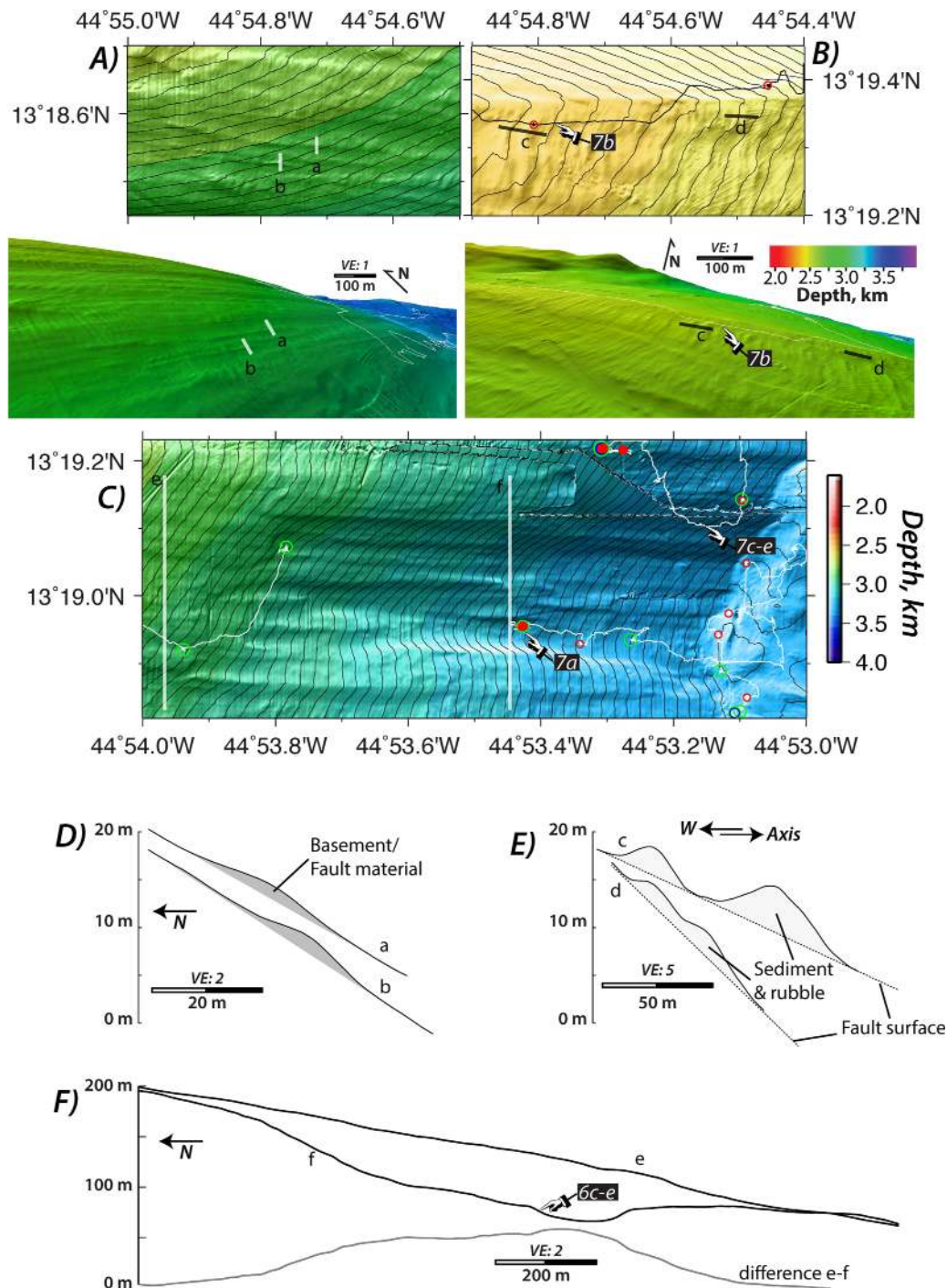
Figure 6. Microbathymetry of the 13°20′N OCC corrugated surface. (A) Detail of detachment fault corrugations in map view (top) and oblique view from the west-southwest (no vertical exaggeration). (B) Rubble ripples overimposed on the corrugations with perpendicular to highly oblique orientations with respect to extension direction, in map view (top) and oblique view from the south-southwest (no vertical exaggeration). ROV tracks correspond to black lines in maps and white lines in 3-D views. (C) Corrugated surface and its termination on the southern flank of the OCC. The morphology shows a depression, elongated in the extension direction, exposing deeper structural levels of the detachment fault zone, and where corrugations are ubiquitous. All maps show 10 m contours. The bathymetric profiles, indicated by letters and lines in Figures 6A–6C correspond to (D) individual corrugations (along lines a and b), (E) the ripples overlying the corrugated surface (along lines c and d), and (F) profiles across the corrugations and the structural low (lines e and f), showing the thickness of the fault zone missing in the area shown in Figure 6C. The shaded areas in Figures 6D and 6E indicate the relief of corrugations and ridges relative to regional slope along profiles. The location of images in Figure 7 is also indicated, as well as ROV tracks and recovered rock types (see legend in Figure 2). Black labels correspond to seafloor images in Figure 7.
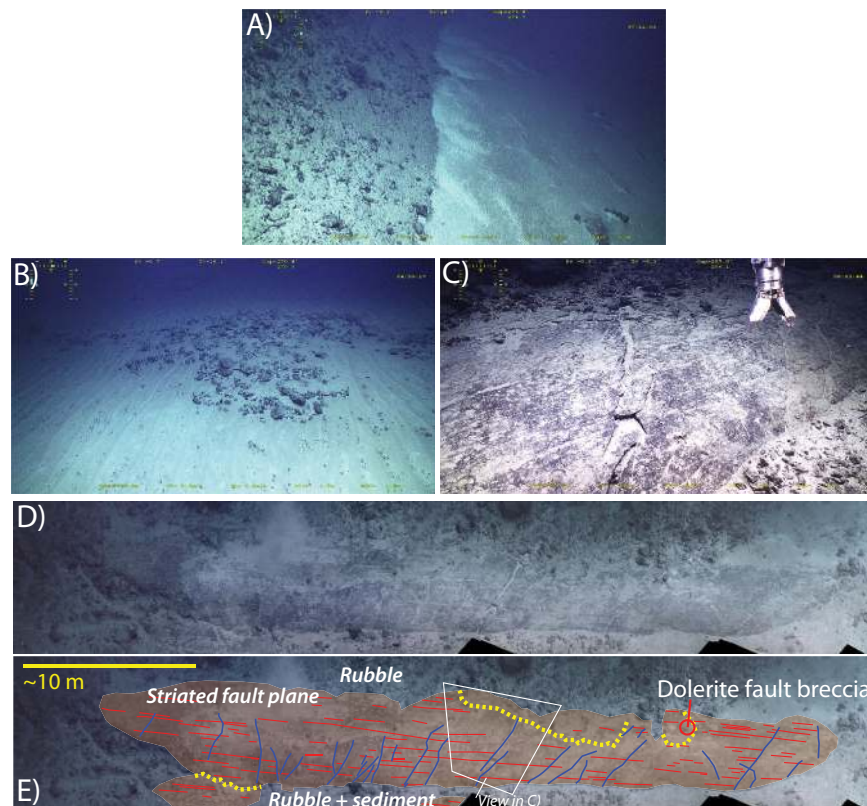
Figure 7. Seafloor images of the 13°20′N corrugated surface. (A) Extension-parallel view (toward the W) of the flank of a corrugation (see location in Figure 6), covered with rubble, and sedimented seafloor at its base (dive 550, field of view ~10 m in foreground). (B) Extension-parallel view (toward the W) of the ridgeward face of a "ripple" ridge crosscutting the corrugation (dive 557, field of view ~15 m in foreground). (C) View of a striated fault plane at the flank of a corrugation (oblique view to striations, see scale and image position in videomosaic in Figure 7E). Striations are subhorizontal and extension-parallel. The fault plane is covered by rubble above, and sediment and rubble at its base. View toward the SSE and see Figure 7E for scale (dive 547). (D) Videomosaic of the ~40 m long striated fault plane in Figure 7C, and (E) the corresponding geologic interpretation (E or ridge axis to the left). Striations are shown in red, fractures at the fault outcrop in blue, and limits of fault surfaces in dashed yellow. The location of a fault breccia sample (diabase) is also indicated.

structures in this terrain that were interpreted as corrugations [*MacLeod et al.*, 2009], we could not identify any morphological features confirming the presence of these corrugations. On both detachments, isolated rock outcrops are primarily basaltic, locally showing in situ pillow lavas at outcrop scale, sometimes interlocking. These outcrops lack lateral continuity at scales greater than 50–100 m, and pillows in some cases appear to be steeply dipping. Gabbro and peridotite samples that are in situ and within the fault zone are scarce, with a single occurrence of sheared peridotite at each of the detachments, in addition to one gabbro and one peridotite sample at the 13°20′N detachment (see supporting information Table S1 and Figure 4).

ROV observations at the summit of the 13°20′N *footwall cutoff* ridge (breakaway, Figure 4B) show that the ridge-facing scarp is steep, showing areas with rubble, sediment, and locally steep, flat fault surfaces (Figure 5B). The ridge edge shows an abrupt transition to the slope dipping away from the ridge axis at ~30°, where the sedimented seafloor shows pillow lavas that are in situ in sedimented seafloor. These pillow lavas do not show downslope elongation, suggesting eruption on subhorizontal seafloor. These ROV observations are consistent with the microbathymetry data (Figure 4B), which shows a sharp contrast between the mass-wasted ridge-ward slope of the breakaway, showing gullies and debris chutes, and the outward-facing slope. The westward slope displays instead a hummocky terrain consistent with volcanic seafloor [*Smith and Cann*, 1990; *Yeo et al.*, 2011], that is also recognizable in the previously acquired near-bottom sonar imagery [*MacLeod et al.*, 2009].

Geologic observations from ROV dives and sampling along the *chaotic terrain* associated with the 13°30′N OCC confirms the presence of hydrothermal deposits (supporting information Table S1), associated with the hydrothermal fields Semenov-1 and Semenov-2 (S1 and S2 in Figure 4A) identified in earlier surveys of
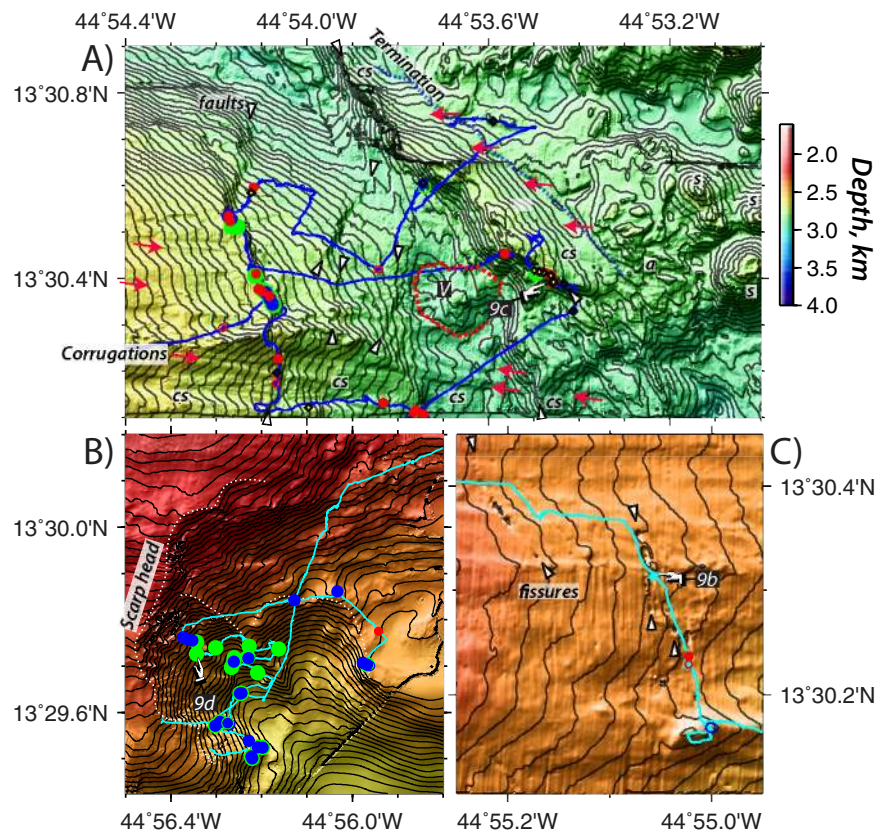
Figure 8. (A) Eastern portion of the corrugated surface associated with the 13°30′N OCC; note crosscutting faults facing both toward and away from the present-day ridge axis (indicated by white triangles), and a portion of the corrugated surface tectonically dissected (*cs*). Corrugations (red arrows) are continuous across faults, that define a graben where fresh lavas and a recent volcanic construction are observed (*V*, dashed red contour). The rift valley floor hosts recent, unfaulted seamounts (*s*), some with clear craters, and the possible remains of the *apron* (*a*) between the volcanic rift valley floor and the termination (see section 4.3). ROV tracks and recovered rock types (see legend in Figure 2) are also indicated. (B) Mass wasting scar on the southern flank of the OCC dissecting the detachment fault. (C) Summit of the 13°30′N corrugated surface showing late fissures (indicated with white-filled triangles). Note straight artifacts in the microbathymetry trending north-south. Black labels correspond to position of seafloor images in Figure 9.

the area [*Beltenev et al.*, 2009; *Pertsev et al.*, 2012]. Our microbathymetry shows that the inactive Semenov-1 hydrothermal mound is 60 m high with a basal diameter of 200 m, and that is situated in an area of flat and smooth seafloor within the *chaotic terrain*. The active Semenov-2 field is located along a ridge-parallel fault scarp bounding a local depression (see Figure 4A); the detailed description of these hydrothermal sites is presented in section 5 below. In contrast, the *chaotic terrain* at the 13°20′N detachment does not show any evidence of past nor present hydrothermal activity.

4.2. Corrugated Surfaces

Both OCCs display a curved fault surface at the seafloor, with what we refer to in this paper as corrugations. These corrugations are observed over a wide range of spatial scales, from broad ones that have widths of ~100 m and amplitudes of tens of m, and that are characteristic of OCCs as they are widely recognized in multibeam shipboard data, to finer-scale corrugations revealed only by the microbathymetric data (Figure 2), that can extend more than ~1 km in the extension direction, and have much smaller amplitudes (a few m). These finer-scale corrugations undoubtedly correspond to the lineaments observed in the sidescan sonar data from OCCs in this same area [*MacLeod et al.*, 2009; *Mallows and Searle*, 2012; *Smith et al.*, 2006], and elsewhere [*Cann et al.*, 1997; *Searle et al.*, 2003], as they have comparable amplitude and wavelengths, and dimensions parallel to plate spreading. In this paper, we refer to as striations the linear features that are visually identifiable along individual fault slip planes both at outcrop and sample scales. The corrugated surfaces on both OCCs share some broad morphological characteristics, including doming both along and across axis, the geometry (width, height length) of individual
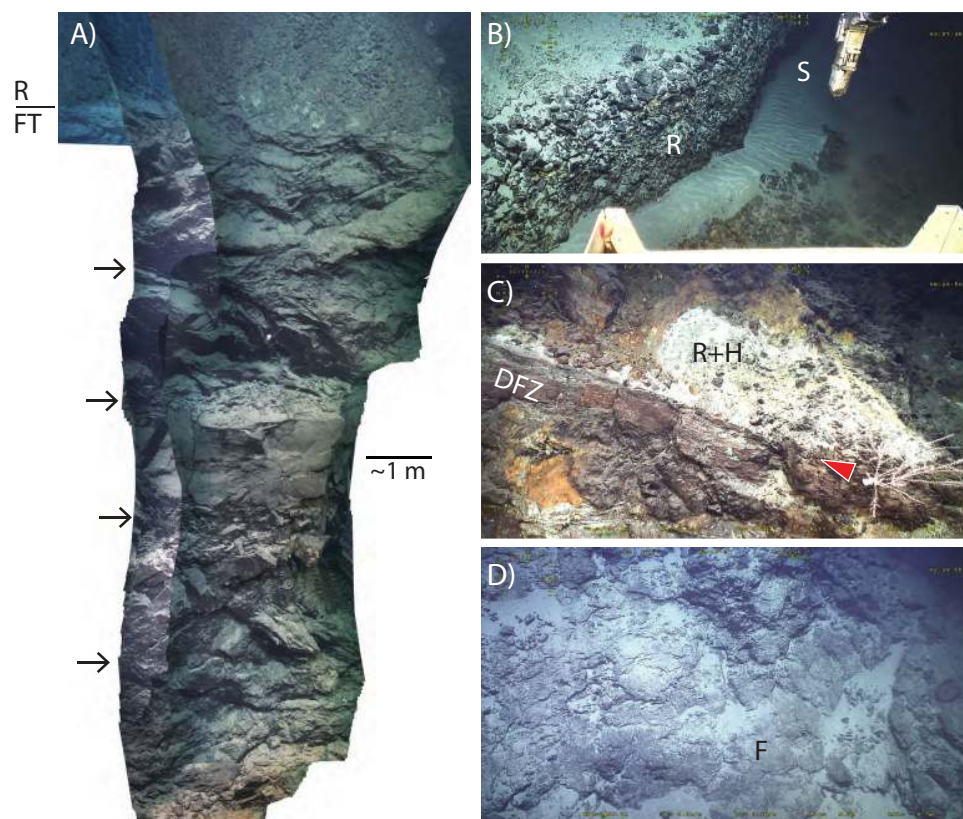
Figure 9. (A) Videomosaic of a ∼10 m high vertical section through the detachment fault zone exposed by a ridge-facing normal fault crosscutting the 13°30′N detachment fault (dive 558). The detachment fault zone shows numerous zones of localized deformation (arrows), with the upper surface of the fault zone clearly identified (FT), overlain by unconsolidated sediment and rubble (R). (B) Late fissure, trending ∼N–S, dissecting the rubble layer (R) and the underlying detachment, and with sediment (S) infill (dive 544, field of view ∼10 m horizontally). (C) Detachment fault zone (DFZ), exposed along the scarp of a fault facing away from the ridge, with its upper surface (red arrow) overlain by rubble. Hydrothermal staining and deposits are observed throughout both in the rubble layer (R+H) and through the detachment fault zone (dive 558, field of view ∼10 m horizontally). (D) Fault plane within the detachment fault (steeply dipping toward the ESE, indicated by the label F) exposed along the mass-wasting scarp dissecting the 13°30′N detachment fault zone (dive 651, field of view ∼15 m horizontally). Locations of images are shown in Figures 8A and B.

corrugations. Our geologic observations and sampling, however, reveal major differences in fault zone composition between these two detachments.

4.2.1. 13°20′N OCC Corrugated Surface

The *corrugated surface* of the southern detachment is curved parallel to the spreading direction, emerging at the rift valley floor at an angle of ∼14°–18°, flattening at its summit, and tilted away from the axis by ∼5° (Figure 3E). The trace of the hangingwall cutoff, where the corrugated fault surface emerges from the seafloor, is curved and reflects the three-dimensional geometry of the corrugated fault (Figures 2C, 3A, and 3C). Off axis the transition with the *chaotic terrain* is abrupt, and marked by an undulating and discontinuous ridge that is subparallel to the present-day ridge axis, that has a relief from a few m and up to ∼10 m (Figure 4B). Seven ROV dives over this corrugated surface provide extensive geological observations and sampling (Figure 2D).

Detachment fault surface corrugations observed in the microbathymetry correspond both to ridges and breaks in the local slope that are subparallel to the extension direction (Figure 6A). These are spaced ∼100–1000 m apart laterally, extending from a few hundreds of meters to ∼2 km in the extension direction. Corrugations have vertical reliefs typically in the range of a few m relative to local relief (Figure 6D) to a maximum of ∼10 m for the most prominent ones (Figure 6B). Close examination of the microbathymetry also shows a series of superimposed, fine-scale ridges oriented from roughly normal to oblique to the corrugations long axis (extension direction, Figure 6B). Vertical relief of these structures crosscutting the corrugations is typically from ∼1 m up to ∼5 m, and are spaced parallel to the extension direction at a few tens of meters.
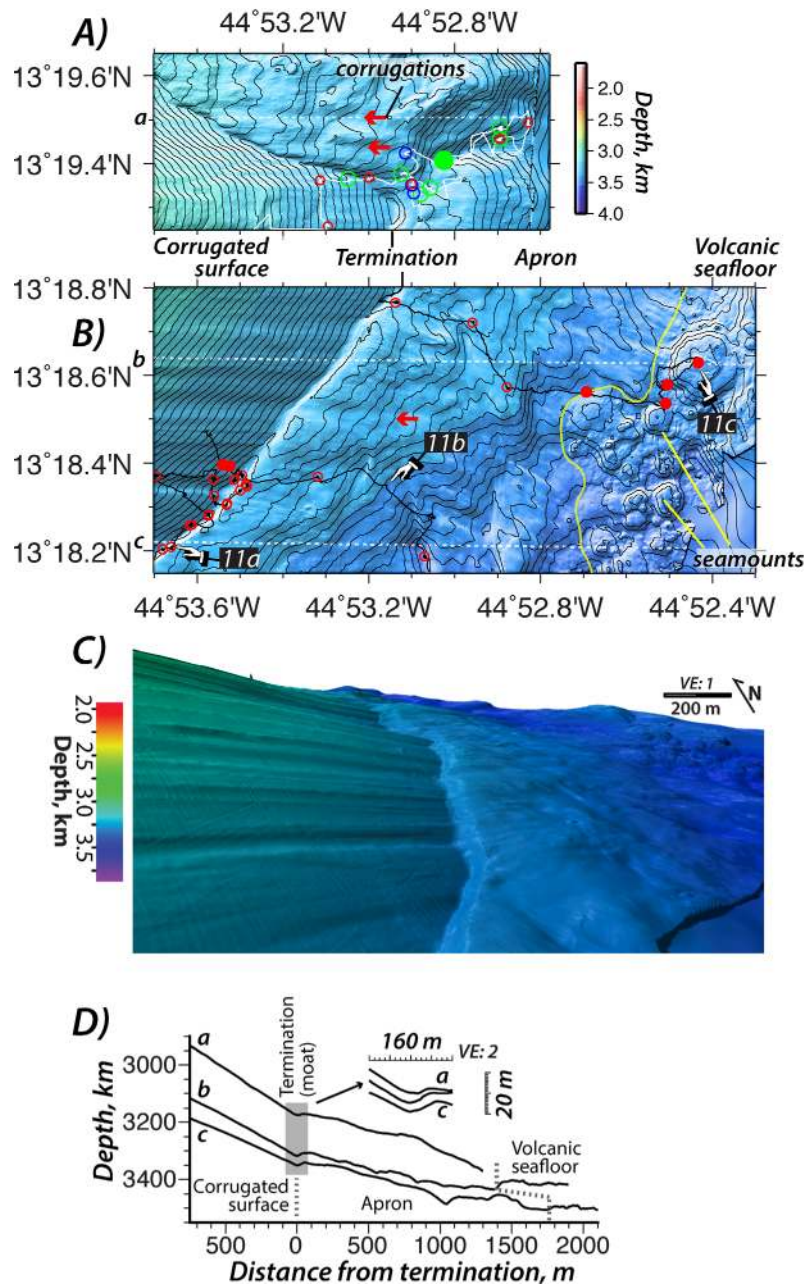
Figure 10. Termination of the corrugated surface and *apron* at both (A) the northern and (B) southern flanks of the 13°20′N OCC. Contact of the *apron* and the volcanic seafloor is also shown in Figure 10B. Contours in Figures 10A and 10B are every 10 m. (C) Oblique view of the moat shown in Figure 10B, with (left) the *corrugated surface* to the west and (right) the *apron* to the east, and the volcanic seafloor and seamounts at the rift valley floor in the background (top right). (D) Extension-parallel profiles across the termination, *apron*, and the adjacent volcanic seafloor. Gray box corresponds to the inset showing the detailed morphology of the moat (profiles have been shifted vertically and stacked for clarity). The termination is laterally continuous, and is associated with a moat that is ∼10–20 m deep, and bound by the ridgeward dipping corrugated surface and a scarp facing the corrugated surface. The *apron* surface shows extension-parallel lineaments that correspond to larger corrugations of the detachment fault (red arrows), in addition to oblique structures associated with its deformation.

They tend to display steeper slopes ridgeward, with an their overall shape that is reminiscent of ripples (Figure 6B).

The 13°20′N detachment surface is structurally continuous and regular (Figure 2C), except for an area immediately south of the eastern tip at the termination (Figure 6C). At this location, we observe a bathymetric low relative to the surrounding detachment fault surface, extending ∼1400 m and up to 500 m in the
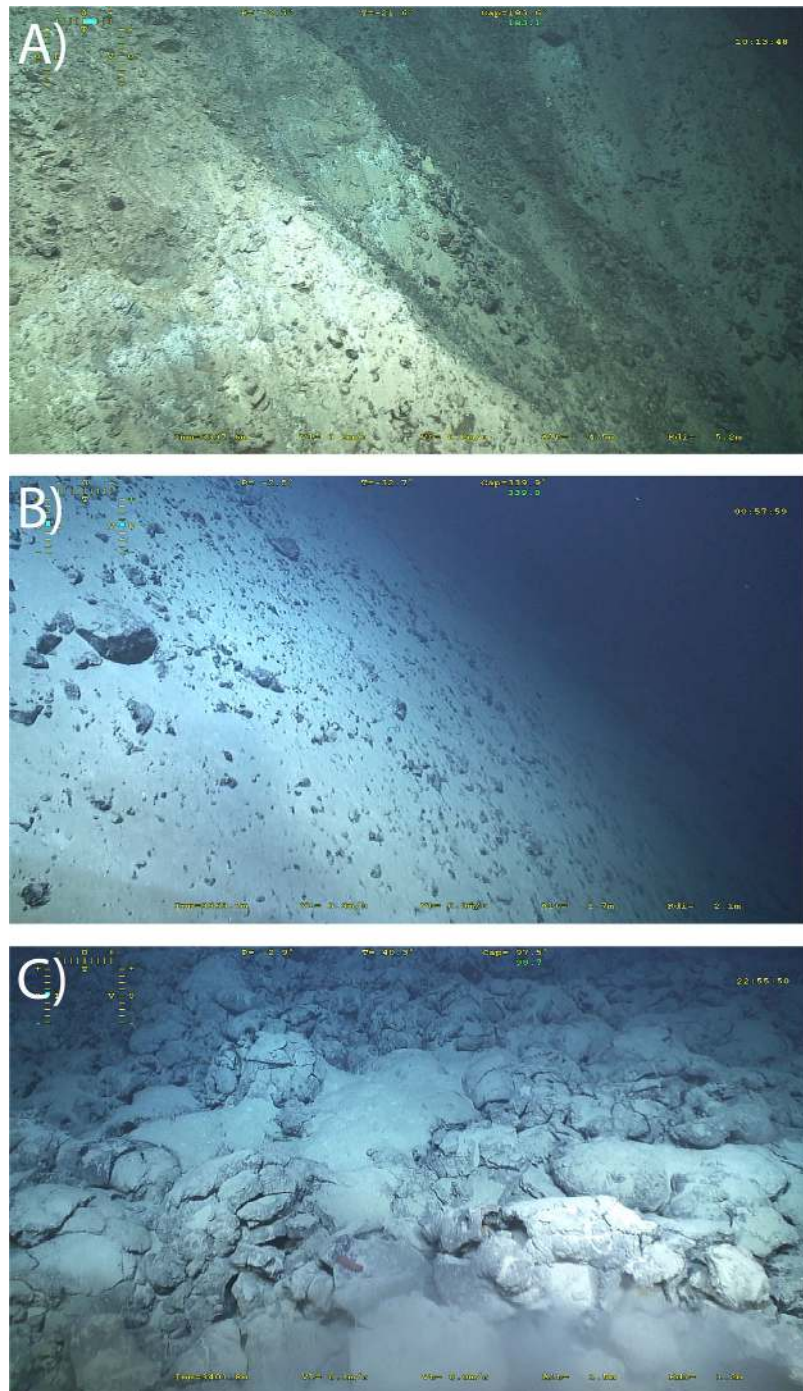
Figure 11. ROV Video captures of the termination, *apron*, and volcanic seafloor at the rift valley floor at 13°20′N. (A) View toward the south of the termination area, showing the scarp facing the corrugated surface and defining the moat at the termination (see inset in Figure 10D, dive 548). The scarp in the view is ~10 m high, exposes unconsolidated rubble in finer-grained material, and displays extensive mass wasting that accumulates at the base of the scarp and over the termination where the corrugated surface emerges. (B) Ridgeward (east dipping) slope of the *apron*, showing a sedimented surface with rubble (dive 548). (C) In situ pillows and lobate basalt flows, showing a light sediment cover, at the summit of a small volcanic seamount immediately adjacent to the base of the *apron* (dive 547, field of view ~10 m). See Figure 10B for location of views.

along- and across-extension directions, respectively, showing corrugations indistinguishable from those of the corrugated surface elsewhere (Figure 6C). Comparison of across axis profiles away from and close to the ridge axis (profiles e and f respectively, Figures 6C and 6F) clearly shows a structural low >70 m deeper than the detachment fault surface surrounding this low (grey line in Figure 6F).
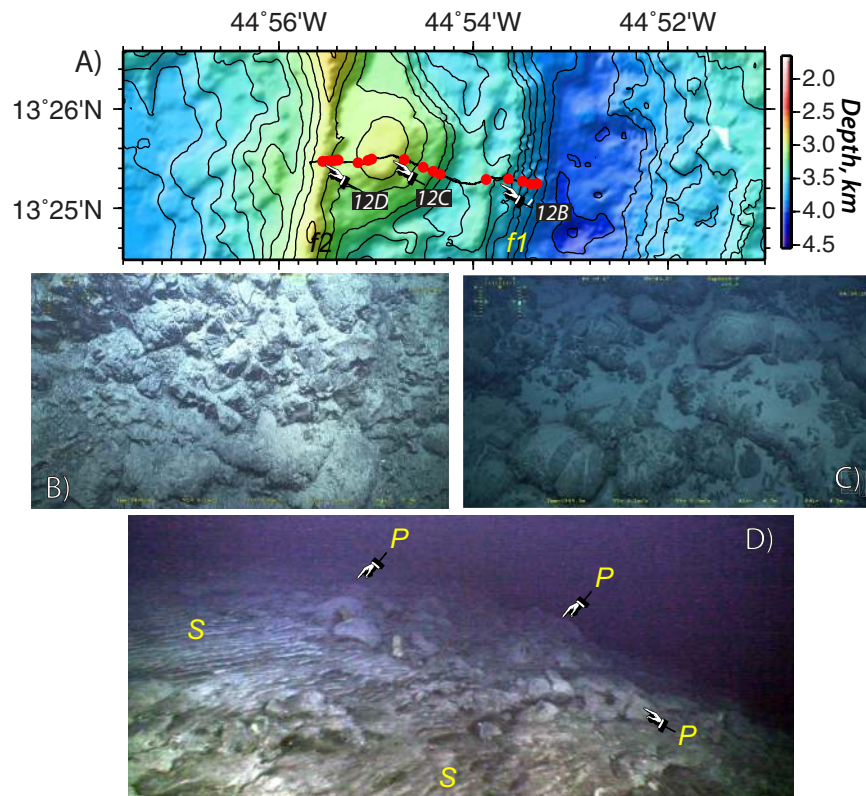
Figure 12. (A) Shipboard multibeam bathymetry of the inter-OCC seafloor showing the track and sampling of ROV dive 545. Labels *f*1 and *f*2 indicate the fault scarps by the rift valley and off axis, respectively. (B) View of in situ pillows (including cross sections) exposed along the base of the rift-bounding scarp (field of view ∼8 m). (C) Lobate and pillow lavas at the summit of the off-axis seamount (field of view ∼10 m). (D) Pillow lavas (P) in sedimented seafloor showing ripples (S), adjacent to edge of Western fault scarp (view to the north-north-east). View taken at the western end of the 545 dive track (field of view in foreground ∼15 m). Location of seafloor images B–D are shown in Figure 12A; black labels).

ROV observations along the corrugated surface show almost continuous blanketing by sediment and rubble. Areas with fine-grained sediment are located primarily in bathymetric lows at the base of slopes or along troughs between ridges that define the corrugations. Unconsolidated rubble is found primarily along the top and flanks of corrugations (Figure 7A). The ripple-like structures across these corrugations (Figure 6B) display packets of rubble on the ridgeward slopes, and fine-grained sediment cover between the ridges (Figure 7B). Sampling of this sediment and rubble blanket yielded primarily basalt, with some samples showing pillow margins, and hosting greenschist grade alteration minerals, in addition to peridotites (see supporting information Table S1 for complete lithological summary).

Locally and along the steeper slopes of the corrugations, we have identified fault planes exposed at the seafloor (Figure 7C). Of the seven outcrops that we have identified, one is on the flank of a corrugation within the structural low shown in Figures 6C and 6F. These outcrops extend ∼30 and ∼100 m in the spreading direction, and up to 100 m laterally. They emerge from the sediment and rubble that otherwise covers the seafloor pervasively across the entire *corrugated surface* and that blankets the corrugations both at their top and their base (Figures 7C–7E). Field observations also suggest that this sediment and rubble cover is thin, and that is locally shed from steeper portions of the corrugated fault surfaces, hence exposing the underlying fault plane at the seafloor. Videomosaics of the fault planes (Figures 7D and 7E), that extend laterally from a few m to a few tens of m, show clear subhorizontal striations along these surfaces. These outcrops also display a complex tectonic structure, with individual striated fault planes terminating against or cross-cutting each other, a geometry reminiscent of that observed at striated fault outcrops on land [*Candela and Renard*, 2012]. These anastomosing fault planes define bodies of rock that are elongate in the extension direction, and flattened subparallel to the overall fault plane orientation and dip. In situ samples of the fault planes are primarily fault breccia with angular basalt clasts. In some oucrops, in addition to the basaltic fault breccias, fault rocks show clasts of serpentinized peridotite together with basalt clasts.

4.2.2. 13°30′N OCC Corrugated Surface

In contrast to the oceanic detachment fault system exposed at the 13°20′N OCC, which is structurally intact (Figure 2B), the 13°30′N OCC detachment surface is disrupted by normal faulting, fissuring, and mass wasting (Figures 2 and 9), but show corrugations that are otherwise morphologically similar to those of the 13°20′ OCC (Figure 9A). Near its termination, the detachment is tectonically dismembered (Figure 9A), with an oblique normal fault scarp facing away from the axis up to ∼100 m high, and a series of smaller (∼10–30 m high) fault scarps facing the ridge axis (Figures 3F and 9A). These faults bound a small local graben cutting the corrugated surface, and isolate a tectonic block toward the termination with the corrugated surface on its ridgeward, northeast slope (cs in Figure 8A).

The 13°30′N corrugated surface is also affected by mass wasting, with coalescing crescent-shaped and steep slump scarps associated with debris deposits downslope (Figures 3B and 8B). The mass wasting features develop on the north and south flanks of the corrugated surface, at the inflexion from subhorizontal to slopes of ∼15° southward and ∼25° northward (Figures 2 and 8B). We also observe fissures crosscut the corrugations at the structurally shallowest areas of the corrugated surface (Figure 8C), that expose both the capping sediment and rubble layer, and the underlying detachment fault zone in their walls (Figure 9B). ROV observations show that these fissures attain widths of up to a few meters across, are up to several tens of centimeter deep, and that are partially infilled with unconsolidated sediment (Figure 9B).

Cross-sections through the detachment fault zone in the footwall are exposed along the scarps of both faults (Figures 9A and 9C) and mass wasting scarps (Figure 9D), and along fissures (Figure 9B) dissecting the 13°30′N OCC. The top of the detachment is subhorizontal at outcrop scale, and ubiquitously covered by a layer of rubble and sediment (Figures 9A and 9C) that is also observed along fissures and faults. The rubble layer thickness is variable, but ROV observations suggest that it can reach up to a few meters (typically <5 m).

The detachment fault zone is exposed along mass-wasting scarps and crosscutting normal faults, and reveals an internal architecture with shear zones varying laterally both in thickness and nature both parallel and perpendicular to the extension direction. Visual ROV observations document discrete fault planes that localize deformation, or damage zones up to a few tens of cm thick that probably correspond to more distributed deformation (Figure 9A). At the scale of outcrops, these high strain shear zones are spaced vertically between a few tens of cm to a few meters (arrows in Figure 9A), and anastomose bounding rock blocks that that visually appear to be undeformed internally.

As at the 13°20′N OCC, the corrugated surface is covered by sediment and rubble, with hydrothermal deposits limited to the active Irinovskoe hydrothermal field (see below). In contrast, the 13°30′N corrugated surface shows sulfide rubble and mounds across much of its surface, corresponding to the hydrothermal fields identified in prior studies [*Cherkashov et al.*, 2016; *Pertsev et al.*, 2012]. The fault scarps also reveal hydrothermal deposits resulting from fluid percolation both through the detachment fault zone and the overlying sediment and rubble (Figure 9C). We have also identified recent volcanics emplaced over this detachment fault surface. These include fresh pillows lavas with fresh glass over the easternmost faulted block of the detachment surface, and the recent volcanic construction (∼30 m high) emplaced within the small graben bound by these later faults, and that seems unfaulted (outlined by red dashed line and labeled *V* in Figure 8A).

4.3. Hangingwall Cutoff and Apron

The hangingwall cutoff (termination) of the 13°20′N corrugated surface toward the ridge axis corresponds to a laterally continuous and well-defined depression or moat (Figures 10A–10C). This moat has variable width, ranging from a few tens of m to ∼250 m, and a vertical relief of ∼10 m in average, reaching ∼40 m locally (Figures 10C and 10D). This moat is also visible in available side-scan sonar data as a bright, acoustically reflective line [*MacLeod et al.*, 2009], and corresponds to the hangingwall cut off, and thus to the structural transition between the footwall (corrugated surface) and the hangingwall. We conducted several ROV dives to obtain geological observations and samples, exploring >8 km of the moat (Figures 2C and 2E). These observations show that the ridgeward, east-dipping western slope of the moat, which corresponds thus to the emerging corrugated detachment surface, is covered by pervasive sediment and rubble, with no outcrop of the detachment fault surface at the seafloor. The eastern moat flank, facing away from the ridge, corresponds to the western limit of the hangingwall (Figures 2C, 2D, 3A, and 10). The steeper and higher scarps show extensive evidence of mass wasting that is likely continuous in time and active at the present time (Figure 11A) This results in rock and debris chutes derived from the hangingwall that

pervasively cover the moat floor. Geologic observations of the moat did not reveal any evidence of recent deformation structures (e.g., newly open fissures or fresh scarps) despite the continued extension and denudation of the detachment system that is inferred.

Both the shipboard and AUV bathymetry show that the seafloor immediately adjacent to the corrugated surface, to the east of the moat, is elevated up to ∼100 m above the adjacent volcanic seafloor at the rift valley floor (Figure 10D). This uplifted terrain defines an arcuate *apron* that follows the curved geometry in plan view of the hangingwall cutoff (Figures (2 and 10)). ROV observations show steep screes that provide evidence of active mass wasting (Figure 11A) westward and toward the center of the moat. The *apron*'s surface also shows a gentler dip than that of the corrugated surface near its termination (∼10°–12° versus ∼15° respectively, Figure 10D). The *apron*'s surface lacks the volcanic morphology found at the rift valley floor (hummocks, volcanic cones), and is instead smoother (Figure 10). The microbathymetry shows two main structures throughout the *apron*: First, there are lineaments parallel to extension and continuous with the larger bathymetric corrugations of the detachment surface (red arrows in Figures 10A and 10B), and second, we observe ridges and troughs dissecting the apron, with orientations relative to the termination that can be both subperpendicular (*apron* by the northern part of the termination, Figure 2C), or subparallel (southern part of the *apron*, Figure 2C). Dives on the apron surface (Figures 10A and 10B) reveals pervasive pelagic sediment cover together with loose rubble and blocks.

The rock types recovered during ROV dives show that the composition of the *apron* is heterogeneous. Along smooth areas lacking marked ridges and troughs, the rubble on the *apron*'s surface is composed primarily of basalt and diabase (Figure 10B). In contrast, sampling during dives along steep flanks of troughs and ridges dissecting the *apron* (e.g., near its western tip, Figure 10A), and along the walls and floor of the moat (termination, Figure 11B), yielded gabbro and peridotite in addition to basaltic rocks. The geological observations both along the *apron* and the eastern wall of the moat (Figure 11B) also revealed outcrops with angular blocks and rocks of variable sizes (up to several m) embedded in an unlithified matrix.

The termination and *apron* at the 13°30′N detachment (Figure 8A) are not clearly defined, likely due to the late faulting dissecting it near axis. Between the rift valley floor seamounts (*s* in Figure 8A) and the faulted block of corrugated surface (*cs* in Figure 8A), we observe and an area with irregular topography (*a* in Figure 8A). In this same area, the termination extends for ∼1 km (dashed line in Figure 8A), and along a local depression that is ∼10–20 m deep, and that may correspond to a now dissected moat similar to that observed at the 13°20′N OCC.

4.4. Axial Valley Floor

The microbathymetry of the axial valley floor immediately adjacent to the terminations of both the 13°20′N and 13°30′N detachment systems reveals a volcanic textured seafloor with both hummocks and volcanic cones. The latter often host summit craters (Figures 8A and 10B). Seamounts can reach ∼500 m in diameter and summit ∼100 m above the surrounding seafloor. Faulting is limited to small scarps (<10 m in vertical offset) dissecting the volcanic cones locally, and fissures. The axial volcanic seafloor adjacent to the 13°20′N was visited at the start of ROV dive 548 (Figure 10B). Sonar maps of this section of the rift valley floor show an acoustic backscatter that is lower than that of the reflective neovolcanic terrain to the North and South of the OCC. This difference in acoustic reflectivity was interpreted to indicate a less magmatic ridge section not resurfaced recently by lava flows [*MacLeod et al*., 2009; *Mallows and Searle*, 2012].

ROV observations showed lobate lava flows at the summit of a flat-topped seamount that are lightly sedimented, and elongated pillows and rubble on its flanks. The seafloor between the base of the volcano and that of the *apron* shows in situ pillow lavas, also with a light sediment cover (Figure 11C). All basalts recovered are fresh and often show glassy rims. The transition from volcanic seafloor to the base of the *apron* at 13°20′N (Figure 10B) shows a rapid although gradual decrease of pillow abundance on the seafloor, and an increase in thickness of the sediment cover and its thickness.

4.5. Inter-OCC Seafloor

The seafloor between the two OCCs is characterized by a ∼4000 m deep basin west of the axial volcanic ridge (Figure 1), bound to the west by a normal fault that extends ∼20 km along axis (labeled *f1* in Figure

12A) and a second one ~3–4 km further off axis to the west (*f2* in Figure 12A), both with a vertical relief of >500 m. The multibeam bathymetry shows that these fault scarps have back tilts of ~10°–15° and 25°–30°, respectively, consistent with progressive increase of the tectonic rotation with distance from the ridge axis, as documented in earlier studies in this and other areas along the MAR [*MacLeod et al.*, 2009; *Schouten et al.*, 2010]. The bathymetry between these two fault scarps also shows a large seamount ~2 km in diameter and ~350 m high (Figure 12A). The summit of this volcano is flat topped and shows a ~10 m deep, elongated crater. Bathymetric profiles across the seamount summit parallel to the extension direction show that the crater rim is subhorizontal, suggesting volcanic emplacement that postdates any tectonic rotation due to faulting. Observations during ROV dive 545 (Figure 12A) show in situ pillow lavas at the summit of the off-axis seamount, that are lightly sedimented but have a fresh visual appearance; samples show glassy rims (Figure 12C). As with the case of the axial valley floor seamounts, the flanks of this off-axis volcano construct show both in situ pillow lavas and basaltic rubble.

The two main fault scarps are morphologically complex, with mass wasting and large-scale fissures, locally exposing in situ pillows and lava tubes. As in the case of the breakaway of the 13°20′N OCC (Figures 4 and 5C), we observe an abrupt transition at the summit of the second scarp to west-dipping seafloor that is heavily sedimented, and locally hosts in situ pillow lavas. All samples recovered along this ROV transect, including those at the seamount described earlier, are basaltic, often show glassy rims, and lack any greenschist facies hydrothermal alteration (supporting information Table S1).

5. Hydrothermal Activity

Previous studies reported an active hydrothermal field (Semenov-2) at the 13°30′N OCC, in addition to numerous inactive vents across the OCC (Semenov-1, 3, 4, and 5), and the presence of massive sulfides that were dredged from the surface the 13°20′N OCC [*Cherkashev et al.*, 2013; *MacLeod et al.*, 2009; *Pertsev et al.*, 2012], without confirming any activity. The ODEMAR cruise identified a water-column Eh and nephelometry anomaly during AUV surveys over the 13°20′N corrugated surface, and ROV seafloor observations confirmed the presence of active venting at the Irinovskoe hydrothermal field. We also extensively studied the Semenov-2 active vent field on the 13°30′N OCC, as well as the fossil hydrothermal deposits throughout the northern OCC (Figures 2A, 2B, 8A, and 9C). Here we provide a brief overview of these results and of the active Irinovskoe and Semenov-2 hydrothermal sites. Detailed description of the active and inactive hydrothermal deposits, and of the chemistry of fluids sampled during the cruise, will be provided elsewhere.

5.1. Irinovskoe Active Hydrothermal Field
The Irinovskoe hydrothermal field, explored during ROV dives 553 and 557, is located on the northern region of the 13°20′N *corrugated surface*, ~1.8 km from the footwall cutoff in the direction of extension (Figures 2C, 2D, and 3A). The microbathymetry of the area shows irregular topography that is typical of hydrothermal deposits elsewhere [*Escartin et al.*, 2015; *Ferrini et al.*, 2008]. Coalescing mounds rise up to ~10–20 m above surrounding seafloor, masking corrugations of the detachment surface over an area ~300 × 200 m in the across- and along-extension directions, respectively (Figure 13A). During two ROV dives we identified two active vents at the summit of hydrothermal mounds, Active Pot and Pinnacle Ridge (Table 1). Both show black smoker fluids venting at ~365°C from ~1 to 2 m high cauldron-shaped structures (Figure 13C) with large exit orifices (several decimeters in diameter), clearly associated with very elevated heat and mass fluxes. We did not observe any associated macrofauna, while bacterial mats and diffuse lower-temperature outflow were limited to the immediate vicinity of these two active vents. The nearby hydrothermal mounds show both fallen and standing hydrothermal chimneys, up to ~10 m in height.

5.2. Semenov-2 Active Hydrothermal Field and Other Sulfide Deposits
Active venting at the Semenov-2 hydrothermal field was first identified in 2007 and later explored with towed camera systems in 2009 during Russian cruises [*Cherkashev et al.*, 2013; *Pertsev et al.*, 2012]. ROV exploration of the site during the ODEMAR cruise shows that the site is located along a fault scarp facing the ridge axis within the *chaotic terrain* west of the corrugated surface, and ~5.5 km from the hangingwall cutoff at the rift valley floor, corresponding to a spreading age of ~470 ka assuming symmetric spreading
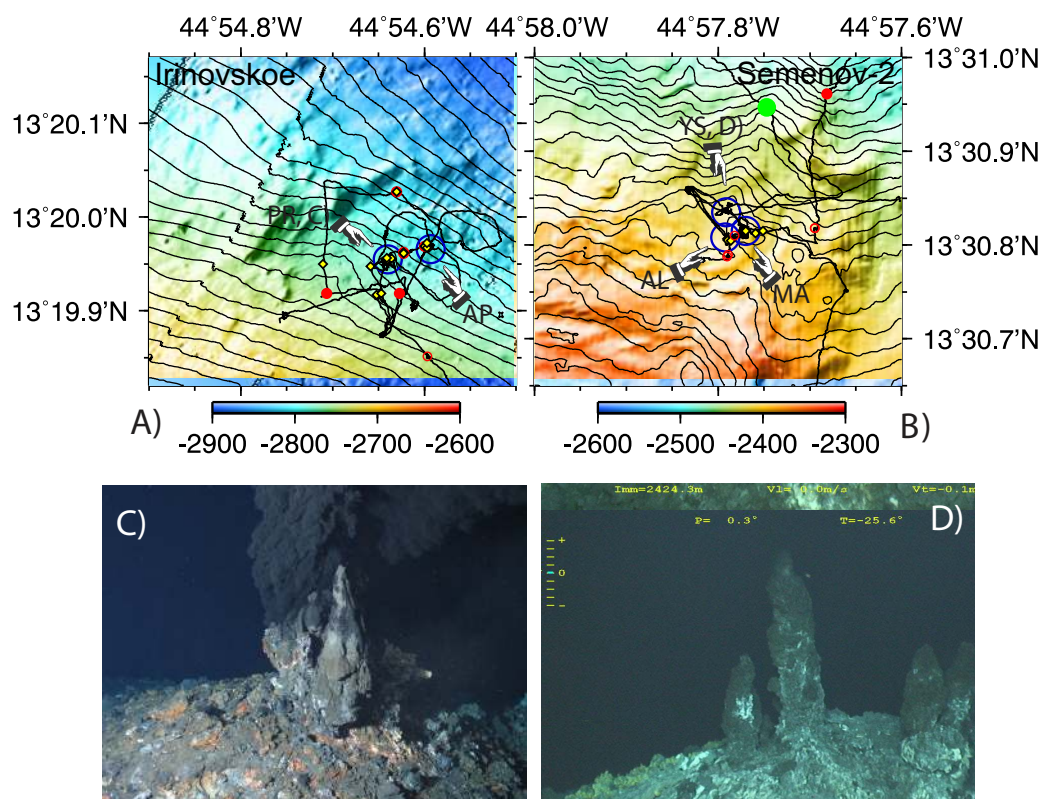
Figure 13. Near-bottom bathymetry of (A) the active Irinovskoe hydrothermal field at the 13°20'N OCC and (B) the Semenov-2 active hydrothermal field at the 13°30'N OCC. Both maps show 10 m contours, and the location of the active fields correspond to the center of the larger dark blue circles: PR: Pinnacle Ridge; AP: Active Pot (see Figure 13C); YS: Yellow Submarine (see Figure 13D); AL: Ash Lighthouse; MA: Michaelangelo. (C) ROV digital photograph of the Pinnacle Ridge vent and associated black smoker type fluids (vent is ~1 m wide), at the Irinovskoe field. ROV dive 553. (D) ROV video capture of the Yellow Submarine site, with ~0.2–0.5 m high chimneys venting clear fluids, at the Semenov-2 field. ROV dive 541.

at a half rate of 12 km/Ma. This field shows several hydrothermal mounds, three of which are actively venting (Michaelangelo, Ash Lighthouse, and Yellow Submarine, Table 1). Hydrothermal fluids are clear to whitish, and vent at temperatures of ~316°C from fragile anhydrite chimneys up to ~2 m tall (Figure 13D). While Michaellangello and Ash Lighthouse mounds show a single chimney structure with several vents, Yellow Submarine shows several chimneys aligned along a ~10–20 m long ridge. Video imagery of these vents show low flow rates when compared with those at the Irinovskoe sites. We observed extended mussel beds and associated bacterial mats the slopes of the Michelangelo mound, extended over an area few tens of meters in diameter, with diffuse hydrothermal outflow and small vents distributed throughout. In contrast, we observed no bacterial mats nor macrofauna at the Ash Lighthouse and Yellow Submarine vent sites.

The ROV tracks conducted over the 13°30'N detachment also revealed ubiquitous hydrothermal deposits over the corrugated fault surface that are more widespread than the limits of the inactive Semenov-3 through 5 as defined in earlier studies [*Pertsev et al.*, 2012]. We also surveyed and sampled the inactive

Table 1. Active Vents Identified During the ODEMAR Cruise[a]				
Name	Latitude	Longitude	Depth (m)	Temperature (°C)
Irinovskoe Hydrothermal Field				
Pinnacle Ridge	13°19.955'N	44°54.640'W	2757	363
Active Pot	13°19.966'N	44°54.593'W	2772	364
Semenov-2 Hydrothermal Field				
Michaelangelo	13°30.815'N	44°57.770'W	2420	317
Ash Lighthouse	13°30.808'N	44°57.792'W	2428	317
Yellow Submarine	13°30.835'N	44°57.791'W	2428	316

[a]We report the maximum temperature measured with the ROV temperature probe inserted at the venting orifice.

Semenov-1 field, which is located further off axis (∼8 km from the volcanic rift valley floor, at seafloor spreading age of 670 ka) within the *chaotic terrain* west of the active Semenov-2, and shows a prominent sulfide mound 200 m in diameter, raising to ∼60 m above surrounding terrain (Figure 4A).

6. Discussion

Microbathymetric data, combined with detailed ROV geological observations and the extensive ROV sampling presented here, allow us to investigate the nature and origin of the different tectonic features described above and associated with the formation of the 13°20'N and 13°30'N. These results demonstrate that surface processes, and in particular mass-wasting, act in conjunction with tectonic processes to shape the seafloor morphology of OCCs, as sketched in Figures 16A–16D. The interaction between these surficial and deeper-seated processes has been fully recognized in geologic studies to date, largely based upon ex situ sampling (e.g., dredging). The data presented here highlight the different tectonic histories of two adjacent OCCs, and show that while the fault rocks from the two detachment fault zones differ in composition, they show a similar corrugated fault surface exposed at the seafloor, resulting from a similar internal detachment fault structure.

6.1. Formation of the Chaotic Terrain: Mass Wasting and Tectonic Rotation of Fault Scarps

Linear ridges that are subparallel to the spreading axis and associated with OCCs are common both along the northern MAR [*MacLeod et al.*, 2009, 2002; *Schouten et al.*, 2010; *Smith et al.*, 2008, 2006], and the Cayman Trough [*Hayman et al.*, 2011], and interpreted as the footwall cutoff (breakaway) of these large-offset faults. Based on our geologic observations and interpretation, we propose that the *chaotic terrain*, between the linear ridges away from the axis and the corrugated surfaces both at the 13°20'N and 13°30'N detachments (Figure 1), corresponds to major fault scarps that developed prior to the seafloor exposure of the corrugated fault surface. These observations also suggest that this zone does not corresponded a disrupted portion of corrugated fault surface, as proposed in an earlier interpretation of sonar data [*MacLeod et al.*, 2009].

Seafloor exposed on the off-axis flank of the breakaway is volcanic, and back tilted due to tectonic extension and associated rotation, as was suggested for these and other similar breakaway ridges along the MAR [*Schouten et al.*, 2010]. This is confirmed by ROV observations at the 13°20'N detachment (Figure 5C), which are consistent with imagery from similar ridges along the MAR at 16°27'N [*Smith et al.*, 2008], and by the volcanic texture observed in sonar imagery [*MacLeod et al.*, 2009; *Mallows and Searle*, 2012]. This volcanic seafloor tilts away from the axis by ∼25°–30° at the 13°20'N, and can reach maximum slopes of 40° [*MacLeod et al.*, 2009; *Schouten et al.*, 2010; *Smith et al.*, 2008]. These observations, together with the inferred footwall rotations of similar magnitude and inferred from paleomagnetic studies [*MacLeod et al.*, 2011; *Morris et al.*, 2009], demonstrate that the formation of these ridges is associated with the development of major faults, such as those bounding the rift valley, inducing significant tectonic rotation [*Buck*, 1988; *Lavier et al.*, 1999].

If breakaway ridges at OCCs indeed correspond to former higher-angle faults, their initial stages of formation may correspond to major scarps that are initially on axis on volcanic seafloor (e.g., axial rift valley bounding faults), and have undergone less tectonic rotation. Figure 14 shows a major rift-bounding fault scarp at the end of the 29°N ridge segment along the MAR [*Escartín et al.*, 1999; *Searle et al.*, 1998], with a back tilt of 10°–20° of the sedimented seafloor off axis, which shows both seamounts and volcanic hummocks (Figure 14A). The fault scarp, which has a slope of ∼20°–30°, shows extensive and pervasive mass wasting, with numerous arcuate head scarps, and by debris deposits at the foot of each scarp in contact with the volcanic seafloor (Figures 14B and 16A). Our data clearly indicate that mass wasting is very efficient near axis, as it has reduced the slope of the fault plane (probably between 45° and 60°) to 20°–30°. The present-day scarp here thus corresponds to an alignment of head scarps of mass wasting structures that have retreated 2–3 km in the extension direction with respect to the now eroded, initial footwall cutoff (Figure 14C). Mass wasting is well documented along the Mid-Atlantic ridge, both along fault scarps crosscutting volcanic seafloor [*Ferrini et al.*, 2013; *Goff and Tucholke*, 1997; *Searle et al.*, 1998; *Tucholke*, 1992], or along faults dissecting detachments and with ultramafic footwalls [*Cannat et al.*, 2013; *Denny et al.*, 2016]. Therefore, active wasting actively reshapes the seafloor and efficiently reduces the slope of scarps toward that of the repose angle of the remobilized rocks to ∼30°–20° [*Cannat et al.*, 2013]. As a result, the angle between back-tilted seafloor and breakaway scarp observed in the bathymetry may not correspond to that
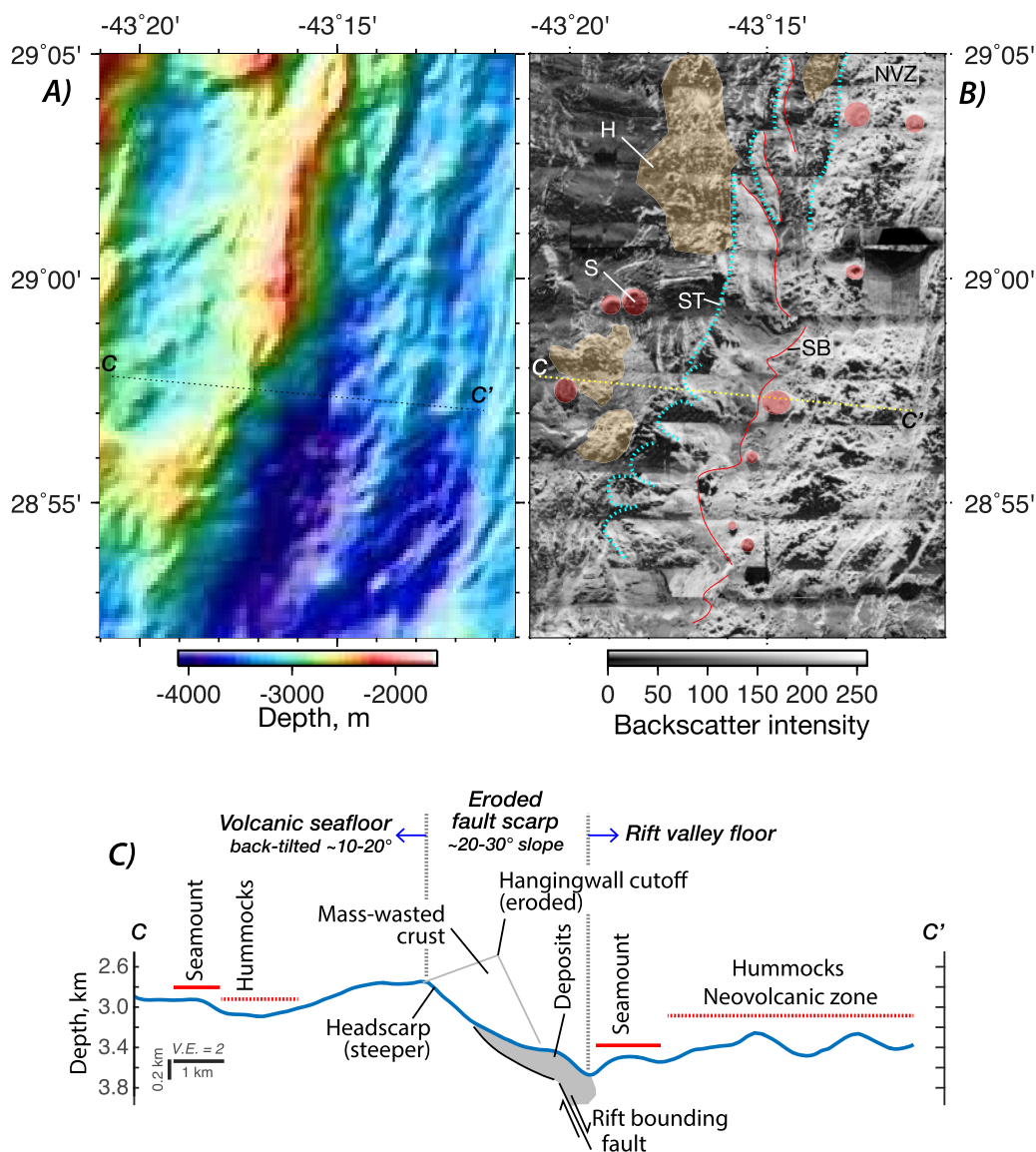
Figure 14. (A) Bathymetry and (B) side-scan sonar image of a major rift bounding wall and rift floor along the 29°N MAR segment. The top of the scarp (ST, light blue dashed line) corresponds to headscarps of mass wasting structures; the associated deposits are in contact and/or cover the volcanic rift valley seafloor at the bottom of the scarp (SB, red line). The seafloor off axis is sedimented but shows both seamounts (S) and hummocks (H) that are also common along the rift floor. (C) Across-axis profile (C-C′ in Figures 14A and 14B) showing back tilt of the older seafloor, and the low angle of the mass-wasted scarp and the steeper headscarp (VE 2:1), and the inferred scarp retreat relative to the original hangingwall cutoff. Mass-wasted material, indicated by gray shading, may accumulate at the base of the scarp and on the hangingwall linked to tectonic subsidence associated with fault extension.

of the original fault angle prior to tectonic rotation [*MacLeod et al.*, 2009], but reflect instead the effects of mass wasting, and in particular the geometry of active or inactive head scarps and the associated talus and debris deposits [*Cannat et al.*, 2013].

Continued extension along major faults is known to result in a progressive reduction in the angle of the exposed footwall surface due to flexural rollover [*Buck*, 1988; *Lavier et al.*, 1999]. After a few kilometers of off-set, seafloor slopes emerging from the detachment root likely become lower than the critical slopes that drive gravitational collapse events (Figure 16B). Mass wasting is thus expected to decrease and ultimately cease, which may subsequently favor the exposure of the actual corrugated fault slip plane observed at many OCCs. Recent observations along the MAR at 16°30′N [*Smith et al.*, 2014] support this hypothesis. In this area, a ∼20 km long fault scarp, with a relief of ∼1 km, shows at its base an incipient corrugated

detachment fault emerging from the rift valley [*R. Parnell-Turner et al.*, 2016; *Smith et al.*, 2014]. This corrugated detachment fault shows an extension of ~1.5 km in the spreading direction, corresponding to ~120 kyr of extension with a spreading half-rate of 12.5 km/Myr. It transitions westward off axis to a mild ~15° scarp with numerous mass-wasting scars and deposits, that are partly shed over and covering the detachment fault itself [*Smith et al.*, 2014]. These observations thus suggest that, at the present time and over the last ~100 kyr or more, the rates of erosion and associated mass wasting cannot fully cover the detachment as it is exhumed at the seafloor.

The interpretation of the *chaotic terrain* of both the 13°20′N and 13°30′N detachments as originally steeper, mass-wasted fault scarps is thus supported both by observations presented in this paper, and those from the 29°N and 16°30′N areas of the MAR summarized above. First, the complex and laterally discontinuous tectonic structure observed here (section 4.1, Figure 4) is consistent with that of mass wasting structures and deposits that run downslope [*Cannat et al.*, 2013], hence extension-parallel, and that are not continuous along axis. Second, more than 75% of the samples collected with ROV are basalt or diabase, consistent with a volcanic upper crust that is crosscut, exposed by near-axis faulting, and subsequently mass wasted (Figures 4 and 5C). Finally, the width of the *chaotic terrain* between the scarp and the initiation of corrugations in this study area (4–5 km, Figures 1 and 4) is consistent with that of major rift wall fault scarps, degraded by significant mass-wasting [*Cannat et al.*, 2013], and with associated retreat (Figure 14). The mass-wasted and rotated fault scarp can also undergo late footwall deformation associated with this flexural response of the lithosphere, including "snapping" and antithetic faulting away from the ridge [*Lavier et al.*, 2000], and observed on surface faults [*Escartín et al.*, 2003a] and footwall microseismicity [*deMartin et al.*, 2007a]. Given that the corrugated surface is subhorizontal and even dips away from the axis, it is necessary that such deformation is accommodated within the *chaotic terrain* of both the 13°20′N and 13°30′N OCCs, as suggested earlier [*MacLeod et al.*, 2009]. However, the AUV microbathymetric coverage is limited (Figure 2), and a detailed tectonic analysis address flexure-related deformation structure is beyond of the scope of this paper. For example, it is not possible to determine if the transition from the *chaotic terrain* to the *corrugated surface* corresponds to the edge of mass-wasting deposits that partially cover the detachment fault surface (Figure 16C), or if it corresponds to a change in the nature and structure of the detachment fault surface originally at depth and that is now exposed at the seafloor. Furthermore, newly acquired microseismic data from this area will provide constraints on the distribution of actively deforming zones, and how these relate to surface structures.

6.2. Formation of Rubble Ridges, Blanketing, and Detachment Fault Exhumation

The hangingwall cutoff at the 13°20′N detachment fault (Figures 2 and 10), and that of the incipient cutoff at 16°36′N [*Smith et al.*, 2014] are both defined by a moat, 10–15m deep, and laterally continuous over several km. This feature is not clearly identified at the 13°30′N OCC owing to the late deformation that cuts this structure (Figure 8A), as discussed above. This geometry of the hangingwall cutoff suggests that there is an efficient mechanical decoupling between the detachment fault surface and the overlying hangingwall material. The ROV observations of this moat at 13°20′N also demonstrate that the unconsolidated debris covering the corrugated detachment fault surface is shed along the *apron* moat wall (Figure 11A), accumulates at the base of the moat onto the detachment fault surface, before being spread out and passively rafted away with continuing extension of the underlying detachment fault (Figures 7B–7D). A similar rubble cover is observed at the incipient 16°36′N corrugated fault surface [*Parnell-Turner et al.*, 2014], suggesting that this blanketing process also operates along the moat observed along this detachment. The presence of rubble over is also documented at other well-studied OCCs with *corrugated surfaces such as* Atlantis Massif [*Blackman et al.*, 2002], and Kane [*Dick et al.*, 2008; *Tucholke et al.*, 2013].

The rubble ridges that crosscut the corrugations are parallel to the trace of the moat (Figures (6 and 7)B, and 15). This geometry suggests that these structures are formed at the hangingwall cutoff at 13°20′N, and is further confirmation of the blanketing of the detachment fault surface by *apron* material. Figure 15 shows an interpretation of both the individual corrugations identified and the geometry and distribution of rubble ridges, distributed across the corrugated surface between the *chaotic terrain* in the west, and the hangingwall cutoff near axis in the east. In some irregularly distributed areas across the detachment surface, individual ridges of length <400 m and averaging ~150 m are superimposed to the microbathymetric corrugations, with a spacing of a few tens of meters to ~100 m. The orientation of the rubble ridges varies along axis and mimics that of the hangingwall cutoff, suggesting that their origin is linked to processes
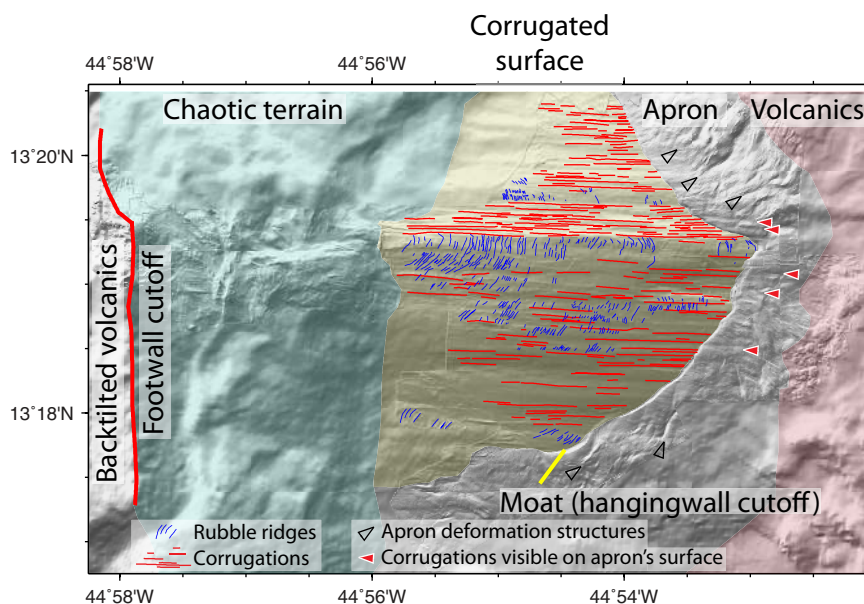
Figure 15. Structural map of the 13°20′N detachment, showing the different domains described. Digitized rubble ridges (blue lines) and small-scale (microbathymetric) corrugations (red lines) over the corrugated surface are also indicated. The *apron* shows a smooth, nonvolcanic morphology, with both ridges and troughs that are oblique to extension and that result from the internal deformation of the *apron* (black open triangles); corrugations of the underlying detachment fault surface, that are draped over by the *apron* (red triangles).

along the moat. The distribution is also irregular across the surface, but areas where sets of these structure are present, their spacing in the extension direction (E-W) varies between a few tens of m and ∼100 m.

We interpret rubble ridges as slump deposits of *apron* material over the corrugated detachment surface (Figure 16E). The sets of ridges show a regular spacing that varies between ∼20 and 100 m (Figure 6B), suggesting a recurrent and episodic emplacement. Assuming that the detachment fault accommodates ∼50% of the full spreading (∼20 km/Myr), this spacing corresponds to a local recurrence of *apron* collapse events along the moat wall of ∼2000–10,000 years. This recurrence may result from a dynamic equilibrium between drag and uplift at the base of the apron in contact with the detachment fault surface, and the mechanical cohesion of the apron resulting in episodic collapse events, that may be triggered seismically. This dynamic equilibrium also maintains the structural continuity of the hangingwall cutoff (moat).

The geometry of the 13°20′N OCC rubble ridges also indicates that the hangingwall cutoff has maintained its overall geometry since the early stages of denudation of the corrugated surface at the seafloor. As the moat also reflects the three-dimensional structure of the OCC, the map in Figure 15 also suggests that the domed shape in the along-axis direction at the present time was acquired during its incipient exposure at the seafloor, ∼500 kyr ago (∼5 km offset). Indeed, examination of the incipient detachment at 16°35′N corrugated surface does show a morphology that is very similar to that at 13°20′N, with an extension of <∼120 kyr (∼1 km offset). Hence, doming in the along-axis direction (Figure 3F) of fault surfaces associated with numerous oceanic detachment faults (e.g., 13°20′N, 13°30′N, Mount Dent, among others), is thus acquired at depth, maintained over long periods of time, and preserved at the seafloor. This suggests that bending flexure postexhumation, as proposed for continental detachments [*John*, 1987; *Yin*, 1991], is absent or very limited at these OCCs. Similar rubble ridges are not apparent in the microbathymetry data from the 13°30′N detachment, although they may be present at the 16°36′N corrugated detachment [see *Smith et al.*, 2014, Figure 4]. This variability in occurrence likely indicates that mass wasting related to rubble ridges may require very specific mechanical conditions that are not always found along the hangingwall cutoff.

In addition to the episodic *apron* collapses recorded by the rubble ridges at the 13°20′N OCC, there is continuous shedding of debris along the moat that blankets the detachment fault surface as it is exposed at the hangingwall cutoff (Figure 16E). This is supported by the lack of detachment fault outcrops along the moat bottom, despite our extensive exploration of this region (Figures 2 and 6), and by the almost
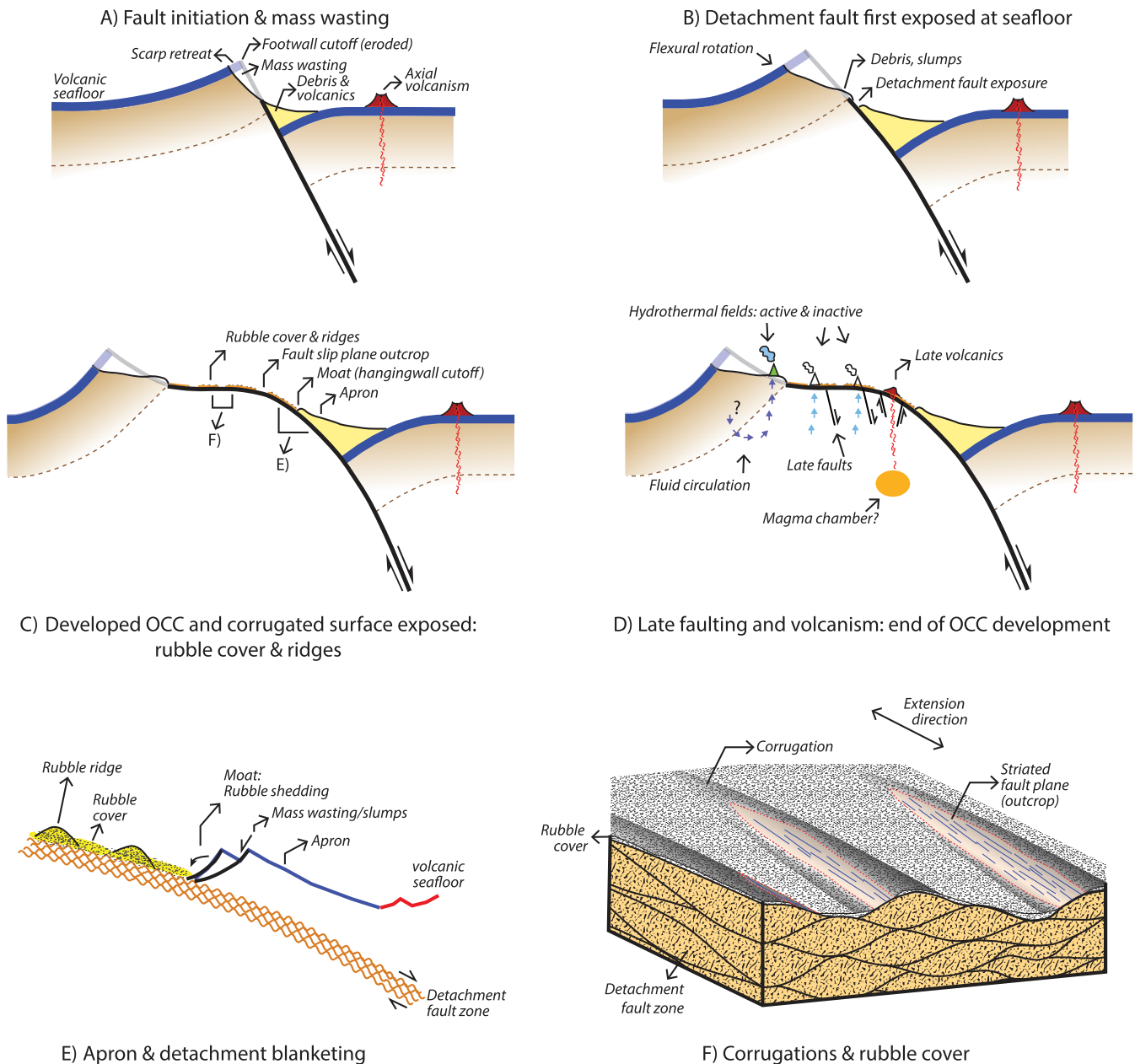
Figure 16. Oceanic detachment fault denudation at the seafloor and links to mass-wasting processes. (A) High-angle normal fault developing near axis shows significant mass wasting, with scarp retreat and debris deposition at its base (e.g., Figure 14). (B) Continued extension results in flexural rotation, and development of an *apron* due to drag by the detachment fault. (C) Corrugated surface exposed at the seafloor and covered by a rubble blanket and rubble ridges originating at the moat (hangingwall cutoff). The location of Figures 16E and 16F are also indicated. (D) Late faulting linked to volcanism and widespread hydrothermal activity throughout the detachment, possibly leading to the termination of detachment faulting. Hydrothermal activity and volcanism is likely due to heat sources (magma chambers?) within the footwall. (E) Detail of the apron and moat, with both continuous shedding of rubble covering the detachment surface, and slumps accumulated as rubble ridges (see Figure 15). (F) Representation of the internal structure of the detachment fault zone (litghtly mottled, coloured), with the anisotropic network of anastomosing fault slip planes. At the surface the corrugations correspond to elongated bodies bound by the fault slip planes, generally covered by a thin layer of unconsolidated rubble (thickly mottled, white), and locally exposing striated planes along the flanks of corrugations (outlined by dashed red lies and stria indicated by blue lines), where the rubble cover has been shed (Figures 7D and E).

ubiquitous sediment and rubble cover observed throughout the corrugated surface of this detachment (Figure 7). Similar rubble cover is observed at 16°36'N [*Parnell-Turner et al.*, 2014, and Figure S1 therein], Kane [*Dick et al.*, 2008], Fuji Dome [*Searle et al.*, 2003], and Atlantis Massif [*Blackman et al.*, 2002].

Rubble ridges of similar lateral extent (∼100 m) and height (a few meter) have been reported at the *corrugated surface* of the Kane OCC [*Tucholke et al.*, 2013]. According to ROV observations here, these ridges run

both parallel and perpendicular to extension, are cemented, and show hydrothemal minerals (Mn oxides, Fe hydroxides). It was thus proposed that the incorporation of these rubble ridges is due to the cementation of the hangingwall material to the surface of the detachment fault owing to low-temperature hydrothermal circulation [*Tucholke et al.*, 2013]. Alternatively, the rubble ridges observed at the Kane OCC may have been emplaced and subsequently rafted in a similar manner to that described above for the 13°20′N OCC, while their mineralization by hydrothermal flow could have occurred subsequently, as inferred for the 13°30′N OCC (see section 5).

The rubble cover is inferred in all cases to be thin (a few meters at most), as it fails to obliterate the low-relief tectonic corrugations of the fault surface (a few m relative to surrounding seafloor, Figure 6D) that are clearly visible in microbathymetry (Figures (2 and 6), and 8) or acoustic backscatter images [*MacLeod et al.*, 2009]. This is also confirmed by limited observations along late, postdetachment fault scarps and fissures dissecting the *corrugated surface* at the 13°30′N OCC (Figure 9). Furthermore, striated outcrops identified along the flanks of corrugations have slopes where the unconsolidated rubble, that covers both the summit of corrugations and the lower areas at their base, has been shed (Figures 7C–7E).

6.3. Nature of Detachment Fault Corrugations
The ROV observations and sampling from the 13°20′N OCC provide probably the best constraints to date to explain the microbathymetric corrugations (Figures 2 and 6) that are superimposed on broader-scale undulations. The origin of the larger undulations have been attributed to different processes, including linked scalloped faults that cut to the surface [*John*, 1987], continuous casting of a ductile (or molten) footwall shaped by a brittle hangingwall [*Spencer*, 1999; *Spencer and Ohara*, 2014], or inherited morphology from an irregular brittle-to-ductile transition [*Tucholke et al.*, 2008], or compression [*Tucholke et al.*, 1998]. The origin of microbathymetric corrugations, with lengths of hundreds of m to a few km (see Figure 15) and unequivocally associated with fault rocks [*Escartín et al.*, 2003a; *MacLeod et al.*, 2011, 2002], is not well understood, and have been attributed to abrasion or deformation marks on a fault surface [*Cann et al.*, 1997].

Our results indicate that the corrugated detachment fault zone comprises an anastomosing network of slip planes, with shorter wavelengths in the along-axis direction than in the extension direction, and over a fault zone thickness of ∼100 m or more. This anisotropic structure is demonstrated by the geometry of individual microbathymetric corrugations, that extend along extension up to 2 km (typically a few hundreds of m) and have a width (across extension) of a few tens of m (Figure 6). Throughout the 13°20′N OCC, the flanks of these corrugations also show fault plane exposures extending up to ∼100 m, systematically displaying sub-horizontal stria consistent with extension. Similar outcrops at the 13°30′N OCC are rare, but striated fault planes were identified both on the corrugated surface itself, and on fault planes within the detachment fault zone exposed in mass wasting scars. This anastomosing set of slip planes delineates phacoidal bodies of rock material that are thus elongated extension-parallel (E-W), and that correspond to the microbathymetric corrugations observed at the detachment fault surface (Figure 16F).

The occurrence of corrugations does not seem to correlate with the nature of the fault zone and the rheology of the lithologies in it, as both the 13°20′N and 13°30′N OCCs show corrugations in the microbathymetry data (Figure 2), as well as striated fault planes in outcrops. These morphological similarities nevertheless occur in fault zones comprising different lithological compositions: whereas the 13°20′N detachment fault is composed primarily of metabasaltic fault breccia, with (only) two ultramafic occurrences, the 13°30′N detachment fault is composed of both peridotite and gabbro, in addition to minor amounts of basalt (Figure 2, supporting information Figure S2 and Table S1). Given the similarity in fine-scale morphology observed at different OCCs (e.g., 16°36′N), and observed in the high-resolution sonar data (e.g., Atlantis Massif and 15°45′N along the MAR, Fuji Dome on the SWIR), we propose that the corrugated surfaces must indicate strain localization within a complex, anisotropic, three-dimensional network of faults, resulting in elongated bodies of rock bound by slip planes. Outcrop observations also suggest that the crosscutting and development of complex fault sets may be analogous to the imbrication of lenses observed in striated continental fault zones [e.g., *Candela and Renard*, 2012], and developed by self-affine process, as proposed for continental faults on the basis of rugosity studies [e.g., *Brodsky et al.*, 2016; *Candela et al.*, 2012]. Lacking deeper sampling of the fault zone and underlying footwall, we cannot determine whether the origin of broader corrugations results from a self-similar strain localization processes operating at larger scales (i.e., larger-scale fault planes linking and crosscutting each other), or to processes proposed by other authors

(e.g., ductile/plastic processes at the base of the lithosphere or the roots of the detachment fault system; see above). Additional information on the extent of the fault at depth, its geometry, and the structure of both the footwall and hangingwall will thus prove to provide critical to provide better constraints and discriminate among the different hypotheses.

Finally, the ubiquitous basaltic fault breccias at the 13°20′detachment fault require a source that is both continuous along axis and stable over time. While dikes intruding the detachment fault zone have been reported at other oceanic detachments [*Blackman et al.*, 2011; *Escartín et al.*, 2003a], and at 13°30′N (this study), there is no evidence of such a process at 13°20′N. Furthermore, these fault-cutting dikes are rare enough that they are unlikely to provide enough material to account for a detachment fault zone with a 75 m thick layer of basalt-dominated fault rocks. A plausible source for this fault material is the base of a dike complex below rift valley floor. As supporting information Figure S2 shows, and owing to the low angle of the fault at shallow depth, there can be an interaction with the hangingwall crust resulting in the deformation and subsequent accretion of this material along the detachment, and its exposure at the seafloor. A detailed analysis of the fault rocks from the 13°20′N OCC, their textures, the associated fluid-rock interactions, and constraints on fault geometry and evolution are in progress and will be presented in a follow-up paper.

6.4. Origin of the Apron: Tectonic Uplift and Internal Deformation

The microbathymetry data from the 13°20′N active detachment (Figure 2B and 15) indicates that the *apron*, which is topographically raised above surrounding volcanic seafloor, corresponds to hangingwall material that is disaggregated and dragged by movement of the underlying detachment fault surface. There are several lines of evidence suggesting that the *apron* is very thin. First, Figures 10 and 15 clearly show that the major extension-parallel undulations and corrugations of the detachment fault surface, which are exposed at the seafloor beyond the hangingwall cutoff, can be followed in the *apron* for ∼1 km toward the ridge axis. Second, the slopes of both the detachment fault at the termination (typically 14°–18°) and of the *apron* (∼15° or less), and the width of the *apron* (1–3 km in the extension direction) provide broad geometric constraints on the *apron* thickness. Assuming a fault plane that is somewhat steeper than at the seafloor (e.g., dipping 20°–25°) we estimate that the *apron* has a thickness of 300 m or less at a distance of 1 km ridgeward from the hangingwall cutoff, and thins toward it. As the *apron* widens away from the 13°20′N OCC center (Figure 15), we expect that it may reach a maximum thickness of 500–700 m below the transition to volcanic rift valley floor (see supporting information Figure S1).

In addition to the continuity of corrugations, the surface morphology of the *apron* also shows a series of ridges and troughs that are oblique to the spreading direction, and that spread radially in the northern part of the 13°20′N *apron* where they are particularly prominent (Figures 2 and 15). These troughs and ridges show an obliquity similar to that of deviating volcanic ridges, which can be attributed to stress reorientations in the vicinity of the active detachment fault [*MacLeod et al.*, 2009], affecting the hangingwall lithosphere above it.

ROV and towed camera observations along the surface of the *apron* at 13°20′N (Figure 11B) and 16°36′N [*Parnell-Turner et al.*, 2014, and Figure S1 therein] show a heavily sedimented surface throughout, with areas of loose rubble. ROV inspection of the ridges and troughs dissecting the *apron* show a greater abundance of rubble and large blocks perched along the steeper slopes, with no continuous outcrop, similar to the observations along the moat where mass wasting exposes well the *apron*'s internal structure (Figure 11A). Observations and sampling (Figure 2 and supporting information Table S1) also indicate that the *apron* is a mélange of predominantly basalt, in addition to minor amounts of peridotite and some gabbroic clasts, all embedded in an unconsolidated matrix. The presence of peridotite clasts in the unconsolidated rubble covering the *corrugated surface* (see Figure 2 and supporting information Figure S2) are consistent with this material being shed from the *apron* along the moat.

6.5. Hydrothermal Heat Sources Within the Footwall

Results of the ODEMAR cruise provide further support to the association between active hydrothermal activity and OCCs [*Escartín et al.*, 2008]. We have conducted extensive mapping of the 13°30′N detachment, where prior studies had mapped inactive hydrothermal deposits in addition to the active Semenov-2 vent field [*Cherkashev et al.*, 2013; *Pertsev et al.*, 2012], and shown that the 13°20′N OCC

hosts the active Irinovskoe hydrothermal field, with outflow through the *corrugated surface*. In both cases, the high-temperature fluids (>300°C), and the associated active and inactive hydrothermal deposits (Figure 13) require a heat source at depth to drive this hydrothermal activity, and over long periods of time. Geochronological studies of hydrothermal deposits from the active Semenov-2 and Irinovskoe sites indeed suggest that hydrothermal activity has been present over the 60–70 ka [*Cherkashov et al.*, 2016], although there is no constrain as to whether the hydrothermal discharge has been continuous or episodic.

Prior models of hydrothermal circulation for hydrothermal systems that are a few km off axis and associated with OCCs (e.g., TAG, Logatchev) have suggested that these systems mine heat from sources at or near axis, and that the detachment fault zone and associated faults channel the hydrothermal fluids laterally toward the discharge zone at the seafloor [*deMartin et al.*, 2007b; *McCaig et al.*, 2010; *Petersen et al.*, 2009]. Geologic observations from the 13°20′N and 13°30′N detachments preclude such a circulation geometry. The detachment fault zone shows pervasive fractures, anastomosing fault zones, and discontinuities (Figures 7D, 8A, 8C, and 9A–9C), that are likely connected with the water column once the detachment is denuded to the seafloor along the footwall cutoff. Such permeability structure would not allow fluids to be transported almost subhorizontally over several km, from the footwall cutoff to the discharge zone at the Semenov-2 and Irinovskoe hydrothermal sites. Furthermore, we would expect that any fluids trapped within this fault zone at depth, if present, would discharge at or near the termination, and along the lateral fluid path. The observations at the moat of the 13°20′N footwall cutoff show no evidence of any fluid flow, and the sediment and rubble covering the *corrugated surface* of this OCC does not show any evidence of hydrothermal activity.

Observations of the hydrothermal structures at the 13°30′N OCC also demonstrate that the hydrothermal fluids percolate and discharge over large parts of the *corrugated surface* instead (Figures 8A and 9C), a model that may apply to the cemented and hydrothermalized rubble documented at the Kane detachment [*Tucholke et al.*, 2013]. We propose that the heat sources responsible for the active hydrothermal systems are located within the footwall, directly underneath these systems. Gravity data suggests that these two *corrugated surfaces* are underlain by high-density material, likely tectonically uplifted gabbro and/or mantle peridotites [*Mallows and Searle*, 2012]. While we have no detailed information of the subsurface structure, those available from other OCCs and their associated hydrothermal systems imply a vertical discharge of fluids instead (Figure 16D), suggesting an emplacement of magma bodies within the footwalls at OCCs that is common. For example, TAG is underlain by a low velocity zone attributed to the discharge zone [*Zhao et al.*, 2012]. Rainbow is underlain by numerous melt lens reflectors, ~3–7 km below seafloor [*Canales et al.*, 2015].

For the 13°30′N OCC, recent faulting dismembering the detachment and the associated volcanism are probably related to its dismantling, owing to the southward propagation of the neovolcanic zone that is found across the left-stepping nontransform discontinuity, between ~13°35′ and 13°40′N the North [*MacLeod et al.*, 2009; *Mallows and Searle*, 2012]. In this tectonic context, the tapped heat source by the Semenov-2 hydrothermal field could then be related to a lateral propagation of the nearby volcanic ridge to the north (see Figure 1). In contrast, the Irinovskoe hydrothermal site is located ~5 km from the neovolcanic zone, and the only plausible source of heat is an intrusion within the footwall, possibly associated with the extension and uplift at the base of the lithosphere and a slightly off-axis magmatic supply captured within the footwall. This off-axis magmatism could ultimately be linked to that responsible for the formation of the seamount observed in the *inter-OCC* terrain (Figures 12A and 12C), and to the interaction with the normal faults that develop toward the north, also affecting the *inter-OCC* terrain (Figure 12A). New seismic data from this area [*R. E. Parnell-Turner et al.*, 2016; *Simao et al.*, 2016] will be critical to determine the location of these heat sources, and understand their origin and link to magmatic processes on axis or elsewhere. These ideas will be further explored in a separate paper that focuses primarily on hydrothermal circulation and associated sulfide deposition within these two OCC's.

7. Conclusions

We present results from an extensive ROV and AUV survey of the 13°20′N and 13°30′N oceanic core complexes, and their associated detachment fault zones. These surveys have provided extensive bathymetry,

visual data, and in situ samples to constrain many aspects of detachment fault formation and evolution. These observations and results demonstrate that surficial processes, including mass wasting of the oceanic crust and deposition of associated debris, are important processes that are intimately linked to the evolution and denudation of oceanic detachment faults. The *chaotic terrain* is often found between the breakaway (footwall cutoff), and the initiation of corrugations. This terrain corresponds to former higher-angle fault scarps, that have been mass wasted and back tilted due to flexural rotation due to the initiation of detachment exhumation.

The detachment fault itself also uplifts hangingwall material near axis, forming a thin wedge with a clear termination (hangingwall cutoff), referred to as an *apron*. This wedge and termination are structures in dynamic equilibrium, reflecting both drag between the fault surface and the *apron*, and decoupling resulting in the continuous and well-defined moat along the termination. Mass wasting processes also operate along this termination moat, and are responsible for the systematic blanketing of the detachment with loose rubble and sedimentary deposits.

Our observations also demonstrate that detachment fault corrugations have a tectonic origin, linked to strain localization, and that their occurrence does not depend on the rock types present in the detachment fault zone. These corrugations result from a complex set of anastomosing and crosscutting faults and shear zones, observed on the seafloor as striated fault planes on the flanks of corrugations. These faults have shorter wavelength undulations in the along-axis direction than those extension-parallel, bounding elongated bodies of rock that are stacked over the thickness of the fault zone, that reaches at least ∼75 m at 13°20′N detachment fault zone. When ruptured along these fault planes, the overall detachment surface shows corrugations that typically have lengths of a few hundreds of m to ∼2 km. These corrugations are directly comparable and widespread over both detachment surfaces, despite significant differences composition of the detachment fault zones; the 13°20′N detachment zone is composed primarily of basalt breccia, likely incorporated from the upper hangingwall, whereas the 13°30′N detachment zone is composed instead of a mixture of gabbro, peridotite, and basalt. Corrugations are thus the result of strain localization processes that are independent of lithology (and rheology of these fault materials).

Finally, our observations confirm the correlation between hydrothermal activity and detachment faulting, with two active hydrothermal fields investigated on both detachments. Our observations preclude lateral transport of fluids from the axial zone to the venting sites, located 10–5 km off axis. Instead, heat sources are likely emplaced within the footwall immediately beneath these sites, possibly linked to the along-axis propagation of the neovolcanic zone that may dissect the 13°30′N detachment, or as an off-axis emplacement of a melt body for the 13°20′N oceanic detachment, similar to that inferred for the off-axis volcano emplaced in the *inter-OCC* crust.

References

Andreani, M., J. Escartin, A. Delacour, B. Ildefonse, M. Godard, J. Dyment, A. E. Fallick, and Y. Fouquet (2014), Tectonic structure, lithology, and hydrothermal signature of the Rainbow massif (Mid-Atlantic Ridge 36°14′N), *Geochem. Geophys. Geosyst.*, *15*, 3543–3571, doi:10.1002/2014GC005269.

Beltenev, V., et al. (2007), A new hydrothermal field at 13°30′N on the Mid-Atlantic Ridge, *InterRidge News*, *16*, 10–11.

Beltenev, V., et al. (2009), New data about hydrothermal fields on the Mid-Atlantic Ridge between 11°–14°N: 32nd Cruise of R/V Professor Logatchev, *InterRidge News*, 18, 13–17.

Blackman, D. K., and J. A. Collins (2010), Lower crustal variability and the crust/mantle transition at the Atlantis Massif oceanic core complex, *Geophys. Res. Lett.*, *37*, L24303, doi:10.1029/2010GL045165.

Blackman, D. K., J. Karson, D. S. Kelley, and S. S. Party (2001), Seafloor mapping and sampling of the MAR 30°N oceanic core complex—MARVEL (Mid-Atlantic ridge vents in extending lithosphere), *InterRidge News*, *10*, 33–36.

Blackman, D. K., et al. (2002), Geology of the atlantis massif (Mid-Atlantic Ridge, 30°N): Implications for the evolution of an ultramafic oceanic core complex, *Mar. Geophys. Res.*, *23*, 443–469.

Blackman, D. K., et al. (2011), Drilling constraints on lithospheric accretion and evolution at Atlantis Massif, Mid-Atlantic Ridge 30°N, *J. Geophys. Res.*, *116*, B07103, doi:10.1029/2010JB007931.

Bonnemains, D., J. Escartín, M. Andreani, C. Mevel, and A. Verlaguet (2015), Dissecting oceanic detachment faults: Fault zone geometry, deformation mechanisms, and nature of fluid-rock interactions, Abstract T43B-3000 presented at 2015 Fall Meeting, AGU, San Francisco, Calif.

Bortnikov, N. S., V. A. Simonov, A. A. Borovikov, V. E. Bel, E. E. Amplieva, A. V. Kotlyarov, and N. V. Bryanskiy (2015), The metalliferous fluid of the hydrothermal sulfide system associated with the oceanic core complex 13°20′N: The Mid-Atlantic Ridge (LA-ICP-MS And Fluid Inclisions), in Oceanic Core Complexes and Hydrothermalism, pp. 80–83, Russian Ridge 2105 Workshop Program, Moscow, Russia.

Brodsky, E., J. Kirkpatrick, and T. Candela (2016), Constraints from fault roughness on the scale-dependent strength of rocks, *Geology*, *44*, 19–22.

Buck, R. W. (1988), Flexural rotation of normal faults, *Tectonics*, *7*, 959–973.

Canales, J. P., R. A. Dunn, R. A. Sohn, G. W. Horning, R. Arai, and M. Paulatto (2015), Seismic reflection imaging of the heat source of an ultramafic-hosted hydrothermal system (rainbow, Mid-Atlantic Ridge 36°10-17′N), Abstract OS41B-02 presented at 2015 Fall Meeting, AGU, San Francisco, Calif.

Candela, T., and F. Renard (2012), Segment linkage process at the origin of slip surface roughness: Evidence from the Dixie Valley fault, *J. Struct. Geol.*, *45*, 87–100.

Candela, T., F. Renard, Y. Klinger, K. Mair, J. Schmittbuhl, and E. E. Brodsky (2012), Roughness of fault surfaces over nine decades of length scales, *J. Geophys. Res. Solid Earth*, *117*, B08409, doi:10.1029/2011JB009041.

Cann, J. R., D. K. Blackman, D. K. Smith, E. McAllister, B. Janssen, S. Mello, E. Avgerinos, A. R. Pascoe, and J. Escartín (1997), Corrugated slip surfaces formed at North Atlantic ridge-transform intersections, *Nature*, *385*, 329–332.

Cannat, M., C. Mével, and D. Stakes (1991), Stretching of the deep crust at the slow-spreading Southwest Indian Ridge, *Tectonophysics*, *190*, 73–94.

Cannat, M., D. Sauter, V. Mendel, E. Ruellan, K. Okino, J. Escartin, V. Combier, and M. Baala (2006), Modes of seafloor generation at a melt-poor ultraslow-spreading ridge, *Geology*, *34*, 605–608.

Cannat, M., A. Mangeney, H. Ondreas, Y. Fouquet, and A. Normand (2013), High-resolution bathymetry reveals contrasting landslide activity shaping the walls of the Mid-Atlantic Ridge axial valley, *Geochem. Geophys. Geosyst.*, *14*, 996–1011, doi:10.1002/ggge.20056.

Cherkashov, G., L. Lazareva, and T. Stepanova (2010a), Massive sulfide deposits at Semyenov cluster: Mineralogy, age and evolution, Miner. Ocean Deep Miner. Min., Joint International Meeting, Joint International Conference, pp. 52–57, St. Petersbourg, Russia.

Cherkashov, G., et al. (2010b), Seafloor massive sulfides from the Northern Equatorial Mid-Atlantic Ridge: New discoveries and perspectives, *Mar. Georesour. Geothechnol.*, *28*, 222–239.

Cherkashov, G., V. Kuznetsov, K. Kuksa, E. Tabuns, F. Maksimov, and V. Bel'tenev (2016), Sulfide geochronology along the Northern Equatorial Mid-Atlantic Ridge, Ore Geol. Rev.

Cherkashev, G. A., V. N. Ivanov, L. I. Lazareva, I. I. Rozhdestvenskaya, M. L. Samovarov, I. M. Poroshina, M. B. Sergeev, T. V. Stepanova, and I. G. Dobretsova (2013), Massive sulfide ores of the Northern Equatorial Mid Atlantic Ridge, *Oceanology*, *53*, 607–619.

Collins, J. A., D. K. Smith, and J. J. McGuire (2012), Seismicity of the Atlantis Massif detachment fault, 30N at the Mid-Atlantic Ridge, *Geochem. Geophys. Geosyst.*, *13*, Q0AG11, doi:10.1029/2012GC004210.

Connelly, D. P., et at. (2012), Hydrothermal vent fields and chemosynthetic biota on the world's deepest seafloor spreading centre. *Nat. Commun.*, *3*, 620.

deMartin, B. J., G. Hirth, and B. Evans (2007a), *Experimental and Seismological Constraints on the Rheology and Alteration of the Lithosphere at Oceanic Spreading Ceners*, Joint Program in Oceanogr., Mass. Inst. of Technol. and Woods Hole Oceanogr. Inst., Woods Hole.

deMartin, B. J., R. A. Sohn, J. P. Canales, and S. E. Humphris (2007b), Kinematics and geometry of active detachment faulting beneath the Trans-Atlantic Geotraverse (TAG) hydrothermal field on the Mid-Atlantic Ridge, *Geology*, *35*, 711–714.

Denny, A. R., D. S. Kelley, and G. L. Früh-Green (2016), Geologic evolution of the Lost City hydrothermal field, *Geochem. Geophys. Geosyst.*, *17*, 375–394, doi:10.1002/2015GC005869.

Dick, H. J. B., M. A. Tivey, and B. E. Tucholke (2008), Plutonic foundation of a slow-spreading ridge segment: Oceanic core complex at Kane Megamullion, 23°30′N, 45°20′W, *Geochem. Geophys. Geosyst.*, *9*, Q05014, doi:10.1029/2007GC001645.

Dick, H. J. B., C. J. Lissenberg, and J. M. Warren (2010), Mantle melting, melt transport, and delivery beneath a slow-spreading ridge: The paleo-MAR from 23°15′N to 23°45′N, *J. Petrol.*, *51*, 425–467, doi:10.1093/petrology/egp088.

Escartín, J., and J. P. Canales (2010), Detachments in oceanic lithosphere: Deformation, magmatism, fluid flow, and ecosystems, *EOS Trans. AGU*, *92*, 31, doi:10.1029/2011EO040003.

Escartín, J., P. A. Cowie, R. C. Searle, S. Allerton, N. C. Mitchell, C. J. MacLeod, and A. P. Slootweg (1999), Quantifying tectonic strain and magmatic accretion at a slow spreading ridge segment, Mid-Atlantic Ridge, 29°N, *J. Geophys. Res.*, *104*, 10,421–10,437.

Escartín, J., C. Mével, C. J. MacLeod, and A. M. McCaig (2003a), Constraints on deformation conditions and the origin of oceanic detachments: The Mid-Atlantic Ridge core complex at 15°45′N, *Geochem. Geophys. Geosyst.*, *4*(8), 1067, doi:10.1029/2001GC000278.

Escartín, J., D. K. Smith, and M. Cannat (2003b), Parallel bands of seismicity at the Mid-Atlantic Ridge, 12-14°N, *Geophys. Res. Lett.*, *30*(12), 1620, doi:10.1029/2003GL017226.

Escartín, J., D. K. Smith, J. Cann, H. Schouten, C. H. Langmuir, and S. Escrig (2008), Central role of detchment faults in accretion of slow-spreading oceanic lithosphere, *Nature*, *455*, 790–794, doi:10.1038/nature07333.

Escartin, J., T. Barreyre, M. Cannat, R. Garcia, N. Gracias, A. Deschamps, A. Salocchi, P.-M. Sarradin, and V. Ballu (2015), Hydrothermal activity along the slow-spreading Lucky Strike ridge segment (Mid-Atlantic Ridge): Distribution, heatflux, and geological controls, *Earth Planet. Sci. Lett.*, *431*, 173–185.

Ferrini, V. L., M. A. Tivey, S. M. Carbotte, F. Martinez, and C. Roman (2008), Variable morphologic expression of volcanic, tectonic, and hydrothermal processes at six hydrothermal vent fields in the Lau back-arc basin, *Geochem. Geophys. Geosyst.*, *9*, Q07022, doi:10.1029/2008GC002047.

Ferrini, V. L., D. J. Shillington, K. Gillis, C. J. MacLeod, D. A. H. Teagle, A. Morris, P. W. Cazenave, S. Hurst, and M. Tominaga (2013), Evidence of mass failure in the Hess Deep Rift from multi-resolutional bathymetry data, *Mar. Geol.*, *339*, 13–21.

Früh-Green, G. L., D. S. Kelley, S. M. Bernasconi, J. A. Karson, K. A. Ludwig, D. A. Butterfield, C. Boschi, and G. Proskurowski (2003), 30,000 years of hydrothermal activity at the Lost City vent field, *Science*, *301*, 495–498.

Früh-Green, G. L., B. N. Orcutt, S. Green, C. Cotterill, and Scientific Expedition 357 (2016), *International Ocean Discovery Program Expedition 357 Preliminary Report: Atlantis Massif Serpentinization and Life*, Int. Ocean Discovery Program, doi:10.14379/iodp.pr.357.2016.

German, C. R., et al. (2010), Diverse styles of submarine venting on the ultraslow spreading Mid-Cayman Rise, *Proc. Natl. Acad. Sci. U. S. A.*, *107*, 14,020–14,025.

Goff, J. A., and B. E. Tucholke (1997), Multiscale spectral analysis of bathymetry on the flank of the Mid-Atlantic Ridge: Modification of the seafloor by mass wasting and sedimentation, *J. Geophys. Res.*, *102*, 15,447–15,462.

Hansen, L. N., M. J. Cheadle, B. E. John, S. M. Swapp, H. J. B. Dick, B. E. Tucholke, and M. A. Tivey (2013), Mylonitic deformation at the Kane oceanic core complex: Implications for the rheological behavior of oceanic detachment faults, *Geochem. Geophys. Geosyst.*, *14*, 3085–3108, doi:10.1002/ggge.20184.

Hayman, N. W., N. R. Grindlay, M. R. Perfit, P. Mann, S. Leroy, and B. Mercier de Lépinay (2011), Oceanic core complex development at the ultraslow spreading Mid-Cayman Spreading Center, *Geochem. Geophys. Geosyst.*, *12*, Q0AG02, doi:10.1029/2010GC003240.

Ildefonse, B., D. K. Blackman, B. E. John, Y. Ohara, D. J. Miller, C. J. MacLeod, and Integrated IODP Expeditions Science Party (2007), Oceanic core complexes and crustal accretion at slow-spreading ridges, *Geology*, *35*, 623–626.

John, B. (1987), Geometry and evolution of a mid-crustal extension fault system: Chemeuevi Mountains, southeastern California, in *Continental Extensional Tectonics*, edited by M. P. Coward, J. F. Dewey, and P. L. Hancock, Geol. Soc. Spec. Publ., 28, 313–335.

John, B. E., and M. J. Cheadle (2010), Deformation and alteration associated with oceanic and continental detachment fault systems: Are they similar?, in *Diversity of Hydrothermal Systems on Slow Spreading Ocean Ridges, Geophys. Monogr. Ser.*, vol. 188, edited by P. A. Rona et al., pp. 175–205, AGU, Washington, D. C.

Karson, J. A., G. L. Früh-Green, D. S. Kelley, E. A. Williams, D. R. Yoerger, and M. Jakuba (2006), Detachment shear zone of the Atlantis Massif core complex, Mid-Atlantic Ridge, 30°N, *Geochem. Geophys. Geosyst.*, 7, Q06016, doi:10.1029/2005GC001109.

Lavier, L., W. R. Buck, and A. N. B. Poliakov (1999), Self-consistent rolling-hinge model for the evolution of large-offset low-angle normal faults, *Geology*, 27, 1127–1130.

Lavier, L., W. R. Buck, and A. N. B. Poliakov (2000), Factors controlling normal fault offset in an ideal brittle layer, *J. Geophys. Res.*, 105, 23,431–23,442.

MacLeod, C. J., et al. (2002), Direct geological evidence for oceanic detachment fauling: The Mid-Atlantic Ridge, 15°45'N, *Geology*, 30, 279–282.

MacLeod, C. J., R. C. Searle, J. F. Casey, C. Mallows, M. Unsworth, K. Achenbach, and M. Harris (2009), Life cycle of oceanic core complexes, *Earth Planet. Sci. Lett.*, 287, 333–344.

MacLeod, C. J., J. Carlut, J. Escartin, H. Horen, and A. Morris (2011), Quantitative constraint on footwall rotations at the 15°45'N oceanic core complex, Mid-Atlantic Ridge: Implications for oceanic detachment fault processes, *Geochem. Geophys. Geosyst.*, 12, Q0AG03, doi:10.1029/2011GC003503.

Mallows, C., and R. C. Searle (2012), A geophysical study of oceanic core complexes and surrounding terrain, Mid-Atlantic Ridge 13°N–14°N, *Geochem. Geophys. Geosyst.*, 13, Q0AG08, doi:10.1029/2012GC004075.

McCaig, A. M., A. Delacour, A. E. Fallick, T. Castelain, and G. L. Früh-Green (2010), Detachment fault control on hydrothermal circulation systems: Interpreting the subsurface beneath the TAG hydrothermal field using the isotopic and geological evolution of oceanic core complexes in the Atlantic, in *Diversity of Hydrothermal Systems on Slow Spreading Ocean Ridges, Geophys. Monogr. Ser.*, vol. 188, edited by P. A. Rona et al., pp. 207–239, AGU, Washington, D. C.

Miranda, E. A., and B. E. John (2010), Strain localization along the Atlantis Bank oceanic detachment fault system, Southwest Indian Ridge, *Geochem. Geophys. Geosyst.*, 11, Q04002, doi:10.1029/2009GC002646.

Morris, A., J. S. Gee, N. J. Pressling, B. E. John, C. J. MacLeod, C. B. Grimes, and R. C. Searle (2009), Footwall rotation in an oceanic core complex quantified using reoriented Integrated Ocean Drilling Program core samples, *Earth Planet. Sci. Lett.*, 287, 217–228.

Nicosevici, T., and R. Garcia (2013), *Efficient 3D Scene Modeling and Mosaicing*, Springer Tracts in Advanced Robotics 87, pp. 1146, Springer, Berlin.

Olive, J.-A., and J. Escartín (2016), Dependence of seismic coupling on normal fault style along the Northern Mid-Atlantic Ridge, *Geochem. Geophys. Geosyst.*, 17, 4128–4152, doi:10.1002/2016GC006460.

Ondréas, H., M. Cannat, Y. Fouquet, and A. Normand (2012), Geological context and vents morphology of the ultramafic-hosted Ashadze hydrothermal areas (Mid-Atlantic Ridge 13°N), *Geochem. Geophys. Geosyst.*, 13, Q0AG14, doi:10.1029/2012GC004433.

Parnell-Turner, R., J. R. Cann, D. K. Smith, H. Schouten, D. Yoerger, C. Palmiotto, A. Zheleznov, and H. Bai (2014), Sedimentation rates test models of oceanic detachment faulting, *Geophys. Res. Lett.*, 41, 7080–7088, doi:10.1002/2014GL061555.

Parnell-Turner, R., H. Schouten, D. K. Smith, 2016. Tectonic structure of the Mid-Atlantic Ridge near 16°30'N. *Geochemistry, Geophys. Geosystems 17*, 2825–2834.

Parnell-Turner, R. E., R. A. Sohn, C. J. MacLeod, C. Peirce, T. J. Reston, and R. C. Searle (2016), Detachment fault behavior revealed by microseismicity at 13°N, Mid-Atlantic Ridge, Abstract T33A-2998 presented at 2016 Fall Meeting, AGU, San Francisco, Calif.

Pertsev, A. N., N. S. Bortnikov, L. Y. Aranovich, E. A. Vlasov, V. E. Beltenev, V. N. Ivanov, and S. G. Simakin (2009), Peridotite-melt interaction under transitional conditions between the spinel and plagioclase facies beneath the Mid-Atlantic Ridge: Insight from peridotites at 13°N, *Petrology*, 17, 124–137.

Pertsev, A. N., N. S. Bortnikov, E. A. Vlasov, V. E. Beltenev, I. G. Dobretsova, and O. A. Ageeva (2012), Recent massive sulfide deposits of the Semenov ore district, Mid-Atlantic Ridge, 13°31' N: Associated rocks of the oceanic core complex and their hydrothermal alteration, *Geol. Ore Deposits*, 54, 334–346.

Petersen, S., K. Kuhn, T. Kuhn, N. Augustin, R. Hékinian, L. Franz, and C. Borowski (2009), The geological setting of the ultramafic-hosted Logatchev hydrothermal field (14°45'N, Mid-Atlantic Ridge) and its influence on massive sulfide formation, *Lithos*, 112, 40–56.

Schouten, H., D. K. Smith, J. Cann, and J. Escartin (2010), Tectonic vs magmatic extension in the presence of core complexes at slow-spreading ridges from a visualization of faulted seafloor topography, *Geology*, 38, 615–618, doi:10.1130/G30803.1.

Schroeder, T., M. J. Cheadle, H. J. B. Dick, U. Faul, J. F. Casey, and P. B. Kelemen (2007), Nonvolcanic seafloor spreading and corner-flow rotation accommodated by extensional faulting at 15°N on the Mid-Atlantic Ridge: A structural synthesis of ODP Leg 209, *Geochem. Geophys. Geosyst.*, 8, Q06015, doi:10.1029/2006GC001567.

Searle, R. C., P. A. Cowie, N. C. Mitchell, N. C. Allerton, C. J. MacLeod, J. Escartín, S. M. Russell, P. A. Slootweg, and T. Tanaka (1998), Fault structure and detailed evolution of a slow spreading ridge segment: The Mid-Atlantic Ridge at 29°N, *Earth Planet. Sci. Lett.*, 154, 167–183.

Searle, R. C., M. Cannat, K. Fujioka, C. Mével, H. Fujimoto, A. Bralee, and L. Parson (2003), FUJI Dome: A large detachment fault near 64 E on the very slow-spreading southwest Indian Ridge, *Geochem. Geophys. Geosyst.*, 4(8), 9105, doi:10.1029/2003GC000519.

Simao, N. M., C. Peirce, M. Falder, T. J. Reston, C. J. MacLeod, and R. C. Searle (2016), Velocity structure of the crust at 13˚N on the Mid-Atlantic Ridge: Implications for crustal accretion and oceanic core complex formation, Abstract T33A-2997 presented at 2016 Fall Meeting, AGU, San Francisco, Calif.

Smith, D. K., and J. R. Cann (1990), Hundreds of small volcanoes on the median valley floor of the Mid-Atlantic Ridge, *Nature*, 344, 427–431.

Smith, D. K., J. Escartín, M. Cannat, M. Tolstoy, C. G. Fox, D. Bohnenstiehl, and S. Bazin (2003), Spatial and temporal distribution of seismicity along the northern Mid-Atlantic Ridge (15°-35°N), *J. Geophys. Res.*, 108(B3), 2167, doi:10.1029/2002JB001964.

Smith, D. K., J. R. Cann, and J. Escartín (2006), Widespread active detachment faulting and core complex formation near 13°N on the Mid-Atlantic Ridge, *Nature*, 443, 440–444, doi:10.1038/04950.

Smith, D. K., J. Escartin, H. Schouten, and J. R. Cann (2008), Fault rotation and core complex formation: Significant processes in seafloor formation at slow-spreading mid-ocean ridges (Mid-Atlantic Ridge, 13 −15° N), *Geochem. Geophys. Geosyst.*, 9, Q03003, doi:10.1029/2007GC001699.

Smith, D. K., et al. (2014), Development and evolution of detachment faulting along 50 km of the Mid-Atlantic Ridge near 16.5°N, *Geochem. Geophys. Geosyst.*, 15, 4692–4711, doi:10.1002/2014GC005563.

Spencer, J. E. (1999), Geologic continuous casting below continental and deep-sea detachment faults and the striated extrusion of Sacsayhuamán, Perú Geol., *27*, 327–330.

Spencer, J. E., and Y. Ohara (2014), Curved grooves at the Godzilla Megamullion in the Philippine Sea and their tectonic significance, *Tectonics*, *33*, 1028–1038, doi:10.1002/2013TC003515.

Tivey, M. A., H. Schouten, and M. C. Kleinrock (2003), A near-bottom magnetic survey of the Mid-Atlantic Ridge axis at 26°N: Implications for the tectonic evolution of the TAG segment, *J. Geophys. Res.*, *108*(B5), 2277, doi:10.1029/2002JB001967.

Tucholke, B. E. (1992), Massive submarine rockslide in the rift-valley wall of the Mid-Atlantic Ridge, *Geology*, *20*, 129–132.

Tucholke, B. E., J. Lin, and M. C. Kleinrock (1998), Megamullions and mullion structure defining oceanic metamorphic core complexes on the Mid-Atlantic Ridge, *J. Geophys. Res.*, *103*, 9857–9866.

Tucholke, B. E., M. D. Behn, W. R. Buck, and J. Lin (2008), Role of melt supply in oceanic detachment faulting and formation of megamullions, *Geology*, *36*, 455–458, doi:10.1130/G24639A.

Tucholke, B. E., S. E. Humphris, and H. J. B. Dick (2013), Cemented mounds and hydrothermal sediments on the detachment surface at Kane Megamullion: A new manifestation of hydrothermal venting, *Geochem. Geophys. Geosyst.*, *14*, 3352–3378, doi:10.1002/ggge.20186.

Wilson, S. C., B. J. Murton, and R. N. Taylor (2013), Mantle composition controls the development of an Oceanic Core Complex, *Geochem. Geophys. Geosyst.*, *14*, 1–18, doi:10.1002/ggge.20046.

Yeo, I., R. C. Searle, K. L. Achenbach, T. P. Le Bas, and B. J. Murton (2011), Eruptive hummocks: Building blocks of the upper ocean crust, *Geology*, *40*, 91–94.

Yin, A. (1991), Mechanisms for the formation of domal and basinal detachment faults: A three-dimensional analysis, *J. Geophys. Res.*, *96*, 14,577–14,594.

Zhao, M., J. P. Canales, and R. A. Sohn (2012), Three-dimensional seismic structure of a Mid-Atlantic Ridge segment characterized by active detachment faulting (Trans-Atlantic Geotraverse, 25°55'N-26°20'N), *Geochem. Geophys. Geosyst.*, *13*, Q0AG13, doi:10.1029/2012GC004454.